Two distinct mechanisms underlie dosage sensitivity in Pumilio1-associated diseases

Salvatore Botta[1,2], Nicola de Prisco[1], Alexei Chemiakine[1], Maximilian Cabaj[1], Vicky L. Brandt[1], Purvi Patel[3], Rajesh K. Soni[3], and Vincenzo A. Gennarino[1,4,5,6,7]

[1]Department of Genetics and Development, Columbia University Irving Medical Center, New York, NY.
[2]Department of Translational Medical Science, University of Campania Luigi Vanvitelli, Caserta, Italy.
[3]Proteomics and Macromolecular Crystallography Shared Resource, Herbert Irving Comprehensive Cancer Center, Columbia University Irving Medical Center, New York, NY.
[4]Departments of Pediatrics and Neurology, Columbia University Irving Medical Center, New York, NY.
[5]Columbia Stem Cell Initiative, Columbia University Irving Medical Center, New York, NY.
[6]Initiative for Columbia Ataxia and Tremor, Columbia University Irving Medical Center, New York, NY.
[7]Lead contact and corresponding author: vag2138@cumc.columbia.edu

Running Title: Mechanisms of PUM1 dosage sensitivity

Abstract

The RNA-binding protein Pumilio1 (PUM1) is associated with distinct diseases: a mild, late-onset ataxia and a severe, wide-ranging neurodevelopmental syndrome. The ataxia patients retain 75% of normal PUM1 levels, the syndromic patients ~50%, but why this should cause such different phenotypes was unclear. Target dysregulation did not explain the difference, so we developed a PUM1 interactome for the mouse brain. This revealed RNA-binding proteins involved in aspects of RNA metabolism not previously associated with PUM1 (e.g., alternative splicing), as well as proteins in unexpected pathways (e.g., anaphase-promoting complex/cyclosome). We focused on a subset of interactors and found that the effects of PUM1 loss on these proteins and their targets varied with brain region and sex. While mild PUM1 loss affected only PUM1-specific targets in patient-derived cell lines, PUM1 haploinsufficiency destabilized these native complexes and altered expression of shared targets in patient cells, mice, and *in vitro*. We propose that dosage-sensitivity can involve distinct mechanisms, and that there may be more intimate coordination among RNA-binding proteins than is readily evinced by more traditional *in vitro* approaches.

Introduction

To respond with agility to a specific perturbation, cells must modify their protein repertoire, much of which is controlled at the post-transcriptional level by RNA-binding proteins (RBPs). RBPs regulate RNA localization, transport, translation, splicing, and decay, and they orchestrate hundreds of pathways that are responsible for proper biological functions (Hentze *et al*, 2018; Keene, 2007b). RBPs can coordinate or compete with each other or exert mutual influence (Dassi, 2017), and they also interact with microRNAs (miRNAs), which are small non-coding RNAs that suppress the expression of their target genes by binding to a short complementary seed region in the 3' UTRs of mRNAs. The RBP and microRNA machinery are particularly important in neurons, whose plasticity demands a rapid local (axonal) response to stimuli despite distance from the nucleus (Mauger *et al*, 2016). Disruptions in RBP function underlie several complex neurological disorders: for example, large CAG expansions in FMRP cause Fragile X syndrome, but milder "premutations" in FMRP cause adult-onset Fragile X-associated tremor and ataxia syndrome (FXTAS) (Lukong *et al*, 2008). The RBPs TDP43 and FUS are both involved in amyotrophic lateral sclerosis, with TDP43 mutations also linked to frontotemporal dementia (Humphrey *et al*, 2020; Ravanidis *et al*, 2018). Despite recent interest in these and other RBPs implicated in neuronal function, we still know relatively little about RBP interactions and regulation (Darnell & Richter, 2012; Khalil *et al*, 2018; Ravanidis *et al.*, 2018).

We recently discovered that the RBP Pumilio1 (PUM1) is involved in two distinct human diseases (Gennarino *et al*, 2018; Gennarino *et al*, 2015). PUM1-associated developmental delay and seizures (PADDAS) is a wide-ranging neurodevelopmental disorder, while PUM1-related cerebellar ataxia (PRCA) is a slowly progressive, pure ataxia with onset in mid-life. Although the severity of the PRCA and PADDAS phenotypes tracks with the levels of functional PUM1 (75% of wild-type levels in PRCA, 40-60% in PADDAS), precisely what is happening at the molecular level was unclear. PUM1 comprises a highly conserved RNA-binding domain composed of eight tandem repeats known as Puf homology domains (HDs), and the mutation that produces mild disease (PRCA), T1035S, lies within this domain and impairs RNA binding—but the most severe PADDAS mutation (R1147W) is outside this domain and does not seem to impair RNA binding (Gennarino *et al.*, 2018; Gennarino *et al.*, 2015). Moreover, the PADDAS phenotype is wide-ranging and variable. The most severe mutation, R1147W, causes small stature, physical dysmorphologies, cognitive and language delays, motor impairments, and seizures starting in infancy. The enormous difference in phenotypic outcomes between mutations in the RNA-binding domain and outside of it, plus the fact that the six then-known PUM1 targets were upregulated to similar extents in the PRCA and PADDAS patient cell lines (Gennarino *et al.*, 2018), led us to hypothesize that PRCA is caused by deregulation of PUM1 targets, but that PADDAS results from

65 disruption of PUM1's interactions with its protein partners along with de-repression of the targets of these
66 complexes.
67 To test this hypothesis would require identifying PUM1 interactors in the mouse brain. Although a
68 great deal is known about the PUMILIO/FBF (PUF) family of RBPs, of which PUM1 and its homolog
69 PUM2 are members, surprisingly little is known about PUM1 function in the postnatal mammalian brain.
70 PUM1 was initially discovered in *Drosophila* for its contributions to embryonic patterning (Lin &
71 Spradling, 1997) and stem cell maintenance (Leeb *et al*, 2014). Studies in fly, worm, and germ cells show
72 that Pumilio proteins regulate mRNA targets through at least three distinct mechanisms: they can
73 collaborate with the miRNA machinery to repress targets (Friend *et al*, 2012; Kedde *et al*, 2010; Miles *et*
74 *al*, 2012); they can recruit the CCR4-NOT deadenylase complex to shorten poly(A) tails and promote
75 mRNA degradation (Temme *et al*, 2014; Van Etten *et al*, 2012; Weidmann *et al*, 2014); and they can
76 antagonize poly(A)-binding proteins to repress translation (Goldstrohm *et al*, 2018). PUM1/2 can also
77 activate certain mRNAs (Bohn *et al*, 2018; Uyhazi *et al*, 2020).
78 Protein interactions in general, and those of PUF family members specifically, can be organism-,
79 transcript-, and even condition-specific (Miller & Olivas, 2011). We therefore took an unbiased approach
80 by using *in vivo* proteomics to identify PUM1's native partners. Because *Drosophila* studies show that
81 Pumilio can change its protein partners in different neuronal types (Muraro *et al*, 2008), we first examined
82 the brain as a whole and then repeated our analyses in three brain regions that most highly express PUM1.
83 We then determined the effect of PUM1 loss on a focused subset of RBP interactors that were the most
84 highly connected within the interactome, using *PUM1* heterozygous and knockout mice and patient-
85 derived cell lines. We also identified targets shared among these interactors and examined their responses
86 to PUM1 insufficiency in mice and cell lines from patients bearing the T1035S and R1147W mutations.
87 Our results support our hypothesis and underscore the need to examine all the interactions an RBP
88 engages in, not just its targets. (Note that, because we deal with both mouse and human proteins in this
89 paper, we will refer to the mouse proteins with lower case (e.g., Pum1) and the human proteins in all caps
90 (PUM1).)
91
92 **Results**
93 **Establishing the Pumilio1 interactome across the adult mouse brain**
94 To identify Pum1 protein partners, we performed co-immunoprecipitation (IP) for Pum1 on whole
95 brains from 10-week-old wild-type mice, followed by liquid chromatography with tandem mass
96 spectrometry (LC-MS/MS, or simply mass spec); we used IP against IgG (IP-IgG) as a negative control
97 (see Materials and Methods). Because of the intrinsic variability of the mass spec technique, we combined

98 and homogenized whole brains from two 10-week-old wild-type mice per sample (1 female and 1 male),
99 aliquoting half of each sample for IP against either Pum1 or IgG, then performed six biological replicates
100 (six samples, 12 mice total) for each mass spec experiment against IP-Pum1 and IP-IgG. Post-IP western
101 blot detected no residual Pum1 from brain tissue, confirming that our protocol recovers virtually all of
102 Pum1 (**Figure S1A**).

103 Principal component analysis (PCA) readily separated the IP-Pum1 interactors from the control IP-
104 IgG (**Figure S1B**). To increase the likelihood that our candidates would prove to be genuine interactors,
105 the proteins had to have at least two unique peptides present in at least five out of six IP-Pum1 samples
106 and also show at least an average >1.5-fold difference between IP-Pum1 and IP-IgG in label-free
107 quantification intensity (LFQ-intensity, see Materials and Methods). Our analysis yielded 412 putative
108 Pum1 interactors (**Figure 1A** and **Table S1**). We incorporated mammalian protein-protein interaction
109 data from CORUM and the Human Protein Atlas by using g:GOSt (g:Profiler; see Materials and
110 Methods) (Raudvere *et al*, 2019) to reveal 22 clusters of functionally related proteins (**Figure 1A**).
111 Among the putative interactors were those that have been previously identified, supporting the validity of
112 our approach. For example, our mass spec identified Nanos1, the mammalian homologue of *Drosophila*
113 Nanos, which was one of the first proteins found to interact with Pumilio during fly development (Wang
114 *et al*, 2001); it also identified Pum2 and Fmrp, which associate with Pum1 in neural progenitor cells
115 (Zhang *et al*, 2017). Some of the identified proteins belong to families previously found to interact with
116 PUM1 *in vitro*, such as Cnot1, which is the central scaffold of the CCR4-NOT complex (Enwerem *et al*,
117 2021; Van Etten *et al.*, 2012). Translation initiation factors (cluster 3) have been found to cooperate with
118 Puf proteins in other species (Blewett & Goldstrohm, 2012), and human PUM2-mediated repression was
119 found to require PABPC1, while our mass spec yielded Pabpc4 (Weidmann *et al.*, 2014). Nanos1 and
120 Pabpc4 have numerous connections among the clusters. Cluster 8, which includes proteins that have been
121 associated with RNA fate regulation, was the most strongly interconnected with other clusters.

122 Most of the proteins, of course, have never been associated with PUM1. Among the candidate
123 interactors with the greatest fold-change were many members of the anaphase-promoting complex
124 (cluster 21). This E3 ubiquitin ligase complex targets substrates for degradation and is essential for
125 neuronal survival (Almeida *et al*, 2005; Gieffers *et al*, 1999; Sivakumar & Gorbsky, 2015). We performed
126 preliminary validation by reciprocal co-IP between Pum1 and Anapc1, which scaffolds the APC/C
127 complex, and between Pum1 and Fzr1, which forms its catalytic pocket (Sivakumar & Gorbsky, 2015)
128 (**Figure S1C, D**). Cluster 11 was also unexpected, as it contains members of both mTORC1 (Rptor, Cad,
129 Tsc1, Tsc2) and mTORC2 (Rictor) pathways, which are involved in a variety of cellular functions from
130 promoting cell growth to autophagy (Liu & Sabatini, 2020). Reciprocal co-IP with Rptor and Cad

131 confirmed interactions with Pum1 (**Figure S1C, D**).

132 Given the plethora of putative interactors to investigate, we repeated the mass spec experiments on
133 the cerebellum, hippocampus, and cortex, where Pum1 is most highly expressed (Gennarino *et al.*, 2015),
134 to see which pathways emerged as predominant. Because our mass spec protocol requires at least 5 mg of
135 protein, we combined cerebellar tissue from eight 10-week-old wild-type mice (4 female and 4 male),
136 performing the experiment in triplicate (for a total of 24 mice); we did the same for cortical tissue. For the
137 hippocampus, we combined tissues from ten wild-type mice (5 of each sex) for three experiments (30
138 mice; see Materials and Methods). As before, we selected proteins with at least two unique peptides and
139 an average of >1.5 fold-change between IP-Pum1 and the IP-IgG. PCA again showed a clear separation
140 of Pum1 samples from the IgG and indicated that the Pum1 hippocampal and cortical interactomes are
141 more similar to each other than to that of the cerebellum (**Figure S2A**). We identified 854 putative Pum1
142 interactors in the cerebellum, 423 in the hippocampus, and 598 in the cortex (**Table S1**). 467 were unique
143 to the cerebellum, 140 to the hippocampus, 229 to the cortex, and 154 unique to the rest of the brain (i.e.,
144 excluding these three regions). Only 88 candidates were shared among these three brain regions and the
145 whole brain (**Figure S2B**, yellow dots; **Figure S2C**). To our surprise, the only brain region to show
146 interaction between Pum1 and Pum2 was the cortex (**Figure S2C**).

147 The region-specific proteins expanded the list of Pum1 interactors in the pathways described initially
148 (**Figure S2D-F**). For example, Cnot1 and Cnot2 turned up in all three brain regions, but Cnot10 appears
149 to be cortex-specific (**Figure S2F**). There were many proteins involved in translation initiation, with
150 Eif3b being specific to the hippocampus (**Figure S2B**). Rbfox1 was specific to the cortex, and Rbfox2 to
151 the cerebellum (**Figure S2B**), consistent with previous work showing that Rbfox1 mediates cell-type-
152 specific splicing in cortical interneurons (Wamsley *et al*, 2018) and that Rbfox2 is needed for cerebellar
153 development (Gehman *et al*, 2012). The brain-region-specific analysis did not yield many additional
154 interactors in the APC/C (**Figure S2D**) or mTOR pathways (**Figure S2E**). It did, however, reveal many
155 pathways that have never been associated with Pum1 (**Table S1**). Taken as a whole, these data suggest
156 that the RNA-silencing, CCR4-NOT, translational initiation, polyA regulation, and splicing machineries
157 are fine-tuned according to brain region or neuronal cell types, whereas the APC/C and mTOR
158 machineries remain fairly consistent, at least across these three brain regions.

159 This is not to say that certain interactions are necessarily limited to these brain regions. They may
160 occur in regions not tested; they may occur across the whole brain, but at levels that did not reach the
161 threshold we set. It could also be that some interactors are expressed more highly in specific brain
162 regions, though this is not the determining factor for the interaction with Pum2, which is expressed to an
163 equivalent degree in all three brain regions (**Figure S2G**).

164 We then performed DAVID Gene Ontology analysis for the hits from both the whole brain and each
165 brain region (**Figure 1B** and **Tables S2**). The dominant categories were ubiquitin ligases (anaphase-
166 promoting complex [APC/C], E2/E3 and Kll-linked ubiquitin) and RBPs involved in various aspects of
167 RNA metabolism (RNA silencing, 3'UTR binding, mRNA stability, transport, and splicing). We decided
168 to prioritize the RBPs in cluster 8 (**Figure 1A**)—Fmrp and Ago2 (involved in RNA silencing), Pum2,
169 Cnot1, and Rbfox3 (an alternative splicing factor)—for three reasons. First, this cluster was the most
170 highly interconnected with other clusters; second, RNA-related categories were prominent in the gene
171 ontology analyses for both whole brain and all three brain regions; and third, these RBPs have been well
172 studied and would allow us to more readily test the consequences of PUM1 loss.
173
174 **Pum1 associates with Pum2, Fmrp, Ago2, and Cnot1 in the absence of mRNA**
175 We first performed co-IP followed by western blot to confirm Pum1 association with Pum2, Fmrp,
176 Ago2, Rbfox3 and Cnot1 (**Figure 2A**, *left panel*). Because Fmrp and Ago2 both bind Mov10 *in vitro*
177 (Kenny *et al*, 2020; Kenny *et al*, 2014), we also blotted for murine Mov10, even though it did not appear
178 among our mass spec results. Mov10 was pulled down with Pum1, likely in concert with Fmrp (**Figure**
179 **2A**). Reciprocal co-IP using antibodies against Pum2, Ago2, Fmrp, Rbfox3, Cnot1, and Mov10 followed
180 by western blot confirmed these associations (**Figure 2B**). To verify the specificity of the antibodies, we
181 co-IPed Pum1 and blotted for all six RBPs in *Pum1*$^{-/-}$ mouse brain and detected none of them (**Figure**
182 **S3A**). As negative controls, we tested other proteins associated with the RISC complex (Ago1 and Ago3)
183 that did not appear in our mass spec data, and our co-IP experiments found no interactions (data not
184 shown).
185 To exclude the possibility that the co-IPs simply recovered other proteins that are co-bound to target
186 RNAs but are not part of the same complex as the protein of interest, we treated the mouse brain samples
187 with RNase and verified that no detectable RNA remained (see Materials and Methods). Pum1 still
188 associated with Pum2, Fmrp, Ago2, and Cnot1 in the absence of mRNA, but not Rbfox3 or Mov10
189 (**Figure 2A**, *right panel*). Interestingly, a previous *in vitro* study observed PUM1 interaction with AGO2
190 only in the presence of RNA in T-REx 293 cells (Sternburg et al., 2018). We repeated the RNase
191 experiments in HEK293T cells, which confirmed our results (except for RBFOX3, which was not
192 detectable in these cells) (**Figure 2C**).
193
194 **Some interactions among these RBPs require PUM1**
195 We next performed reciprocal co-IP in wild-type and *Pum1*$^{-/-}$ 10-week-old mouse brains for Pum2,
196 Ago2, Fmrp, Cnot1, Rbfox3, and Mov10. Pum2 interacted with Cnot1 only in the presence of Pum1

197 (**Figure 3A**). Unexpectedly, Fmrp associated with Mov10 and Rbfox3 only in the presence of Pum1
198 (**Figure 3B-D**). Fmrp and Cnot1 did not associate in the wild-type brain (**Figure 3B**, *left*) but they did so
199 in the absence of Pum1 (**Figure 3B**, *right*). Ago2 associated with Pum1, Fmrp, Cnot1 and Mov10 in wild-
200 type brain, but in the absence of Pum1 it no longer interacted with Fmrp or Mov10 (**Figure 3E**). Rbfox3
201 associated with Cnot1 (**Figure 3C**) but not *vice versa* (**Figure 3F**). IPs against Pum2, Ago2, Fmrp, Cnot1,
202 Rbfox3, and Mov10 with and without RNase treatment in wild-type and *Pum1*$^{-/-}$ mouse brains (**Figure**
203 **S3B-G**) confirmed that, in the absence of Pum1, these interactions require RNA.
204 These results underscore the importance of examining RBP interactions *in vivo*, in specific contexts,
205 with and without RNase treatment. For example, previous work showed that AGO2, PABPC1, GW182
206 and CNOT1 interact with nuclear EGFR to regulate VEGF signaling in tumor cell lines (Dittmann *et al*,
207 2017), but neither GW182 nor EGFR turned up in either our whole-brain or regional interactomes. In fact,
208 none of GW182's three mammalian paralogues (Tnrc6A, Tnrc6B, or Tnrc6C), which interact with all
209 four human AGO proteins, was pulled down in our mass spec against Pum1 (**Table S1**).
210 In murine neurons, therefore, Pum1 associates with Pum2, Fmrp, Ago2, and Cnot1, with or without
211 RNA (**Figure 3A-F** and **Figure S3B-G**). Pum1 seems to be required for association between Fmrp,
212 Mov10 and Rbfox3, and between Ago2 and Fmrp, Mov10, and Cnot1. In the absence of Pum1, the
213 associations between Pum2, Fmrp, Ago2 and Cnot1 require RNA (**Figure S3B-G**).
214
215 **Pum1 loss alters RBP levels by brain region and sex**
216 If these are *bona fide* interactors of Pum1, then we would expect loss of Pum1 to alter their
217 abundance. *Pum1* heterozygous and knockout mice showed changes in the quantities of Pum2, Ago2, and
218 Mov10 proteins across the brain (**Figure S4A**), but only *Pum2* showed changes in mRNA levels (**Figure**
219 **S4B**). Interestingly, Ago2 and Mov10 levels fell only in male mice (**Figure S4A**), so we decided to
220 pursue this sex difference by brain region. We quantified Pum2, Fmrp, Ago2, Rbfox3, Cnot1 and Mov10
221 in the cerebellum, cortex, and hippocampus. We first measured Pum1 mRNA and protein levels to
222 confirm the reduction of Pum1 in our *Pum1*$^{+/-}$ or *Pum1*$^{-/-}$ mice in each brain region (**Figure 4A-C,** and
223 **S5A**). Pum2 protein levels rose in all three brain regions, as did its mRNA (**Figure 4A-C,** and **S5A**).
224 Fmrp protein expression was upregulated in all three brain regions in male KO mice, but in female
225 KO cerebella Fmrp was reduced by almost 70% (**Figure 4A**). (We should note that sex differences in
226 Fmrp expression have been previously reported (Singh *et al*, 2007; Singh & Prasad, 2008).) Three other
227 proteins also showed divergent responses to Pum1 loss according to sex and brain region: Ago2 (up in
228 female but down in male cerebella, with the opposite pattern in hippocampus and cortex), Rbfox3 (in the
229 hippocampus), and Cnot1 (in the cerebellum) (**Figure 4A-C**). None of them showed any changes in

230 mRNA levels (**Figure S5A**), despite the fact that *Fmr1* and *Cnot1*, like *Pum2*, have a Pumilio Response
231 Element (PRE) (Zamore *et al*, 1997)—sometimes known as a Pumilio Recognition Element (PRE) or
232 Pumilio Binding Element (PBE)—in their 3'UTR. It may be that the loss of Pum1 causes sex- and region-
233 specific reorganization of these complexes, or that there are additional sex-specific Pum1 interactors.
234

235 **Pum1 loss dysregulates Ago2 and the microRNA machinery in mouse cerebella by sex**

236 Since loss of Pum1 function has deleterious effects on the cerebellum in both mice (Gennarino *et al.*,
237 2015) and humans (Gennarino *et al.*, 2018), we were curious to know whether the divergence of Ago2
238 protein levels in males and females extended to cerebellar miRNAs. We performed miRNAseq.
239 Hierarchical heatmap clustering of miRNA expression in *Pum1*$^{-/-}$ and WT male and female cerebella at 10
240 weeks of age revealed that the expression of 166 miRNAs (**Table S3**) diverged between the two sexes in
241 parallel with Ago2 expression (**Figure 4D**).

242 To examine the functional consequences of this Ago2/miRNA dysregulation, we looked at the
243 expression of downstream targets that are co-bound by those miRNAs in 10-week-old wild-type and
244 *Pum1*$^{-/-}$ male and female cerebella. We first selected all the miRNAs with at least a 25% change in
245 expression in either direction, for a total of 19 miRNAs. Using TargetScan and CoMeTa (Agarwal *et al*,
246 2015; Gennarino *et al*, 2012) we identified 6832 putative targets that are co-bound by at least 2 out of 19
247 possible miRNAs. To reduce this list to a more manageable size for testing expression changes by qPCR,
248 we prioritized targets that are co-bound by at least 8 miRNAs, for a total of 49 putative targets. *Pum1*$^{-/-}$
249 male and female cerebella showed gene expression changes for 44 out of these 49 targets, which
250 correlated with the sex-dependent differences in Ago2 levels (**Figure 4E**, **S5B** and **Table S4**).
251

252 **The top targets of Pum1, Pum2, Fmrp, Ago2, and Rbfox3 are shared**

253 So far our *in vivo* proteomics results seem to be borne out by changes in the levels of protein
254 interactors upon loss of Pum1. Ideally, we would purify recombinant proteins to perform gel filtration
255 assays to get a better handle on the nature of the interactions, but Pum1 is difficult to purify because it is
256 prone to aggregation (Miller & Olivas, 2011). If the complexes Pum1 forms with these RBPs are
257 physiologically relevant, however, then they should co-regulate at least some of the same mRNA targets.
258 Indeed, one corollary of the "regulon theory," which posits that mRNA targets in the same pathway are
259 co-regulated (Blackinton & Keene, 2014; Keene, 2007a, b; Keene & Lager, 2005), is that there should be
260 a discernible set of RBPs that do the co-regulating.

261 To test this hypothesis, we downloaded and reanalyzed all the high-throughput sequencing UV-
262 crosslinking and immunoprecipitation (HITS-CLIP) data that is available from the murine brain.

263 Fortunately, this data exist for Fmrp (Maurin *et al*, 2018), Ago2 (Chi *et al*, 2009), Rbfox3 (Weyn-
264 Vanhentenryck *et al*, 2014), Pum1, and Pum2 (Zhang *et al.*, 2017). Then, to determine whether and how
265 much the targets overlap, we performed gene set enrichment analysis (GSEA) (Subramanian *et al*, 2005).
266 GSEA is a method for determining whether members of a particular class of genes from set *S,* such as the
267 targets of a particular RBP like Pum1, are randomly distributed throughout another gene set list *L*, which
268 is ranked (in this case) according to reads per kilobase of transcript, per million mapped reads (RPKM).
269 Genes from *S* that are enriched (over-represented) at the top of *L* are expressed more than would be
270 expected; the converse is true for genes over-represented at the bottom of *L*. Here, we performed pairwise
271 GSEA analysis using Fmrp as the basis for comparison (because it has the largest dataset) and Pum1,
272 Pum2, Ago2 and Rbfox3. As negative controls, we used HITS-CLIP data from mouse brain for four
273 RBPs that did not show up as Pum1 interactors in our mass spec: Mbnl2 (Charizanis *et al*, 2012), Nova
274 (Zhang *et al*, 2010), Apc (Preitner *et al*, 2014), and Ptpb2 (Licatalosi *et al*, 2012).
275 Strikingly, Pum1 HITS-CLIP targets were preferentially distributed in the top 5th percentile of all
276 Fmrp targets, with an enrichment score (ES) of 0.93 (the maximum is 1) and a FDR of 0 (**Figure 5A,** *blue*
277 *line represents ES*). Pum2, Ago2, and Rbfox3 showed nearly identical patterns (**Figure 5A**). There was
278 no significant overlap between the targets of Fmrp and those of any negative control (Nova had the
279 highest ES, but this was only 0.36 with a rank max of 45th percentile and FDR=1; **Figure 5B**).
280 To ascertain whether the highest-ranking Fmrp targets correspond to the genes with the highest
281 probability of being Pum1 targets, we performed a more detailed GSEA. We first divided the Fmrp
282 ranked target list into 10 equal bins according to percentile. We then repeated GSEA of Pum1 HITS-CLIP
283 data for each bin and found that 648 of the 1194 identified Pum1 targets (54%) are in the top 10th
284 percentile of Fmrp targets, with an ES of 0.8; moreover, this was the only statistically significant bin
285 (**Figure 5C**). This was also true for Pum2, Ago2, and Rbfox3 (**Figure 5C**). Neither Pum1, Pum2, Rbfox3,
286 Fmrp, nor Ago2 targets were enriched among any of the target lists of the negative controls ranked by
287 RPKM (**Figure S6A,** and data not shown).
288 We then performed the corresponding analysis using the Pum1 target list as the basis for comparison
289 instead of the Fmrp list. We ran GSEA on each of the four Pum1 partners against the list of Pum1 target
290 genes (again ranked by RPKM), and each partner's targets are within the top 20% of the Pum1 list
291 (**Figure 5D**). Specifically, Fmrp's targets reside in the top 10th percentile (with an ES of 0.81), Pum2's
292 targets within the 16th percentile (ES=0.9), Ago2's targets within the 18th percentile (ES=0.76), and
293 Rbofx3's targets within the 19th percentile (ES=0.67). The four RBPs used here as negative controls have
294 a minimum rank at the 37th percentile, and the best ES was 0.26 for Apc; none of the five reached
295 statistical significance (**Figure 5D**). These analyses demonstrate that there is substantial overlap among

296 the highest-ranked targets of Pum1, Pum2, Fmrp, Ago2, and Rbfox3.

297 We then decided to look at the targets shared by Pum1, Pum2, Ago2, and Rbfox3 and see how they
298 distribute within Fmrp. The result was striking, with an ES of 0.93 falling within the top 5th percentile
299 (**Figure 5E**); 141 out of 175 common targets were within the top 10th percentile (bin 1) of Fmrp targets,
300 with 99 within the top 5th (**Figure 5F** and **Table S5**). This contrasts with the negative controls, for which
301 the best ES was 0.41 within the top 40th-60th percentile (**Figure 5G**). DAVID gene ontology analysis of
302 those 175 common targets between Ago2, Pum1, Pum2, Fmrp, and Rbfox3 revealed pathways enriched in
303 neurons and axonal projections (**Figure S6B** and **C**). Previous studies have shown that Pum1 and Pum2
304 cooperate with the microRNA machinery to suppress certain targets (Gennarino *et al.*, 2015; Kedde *et al.*,
305 2010). Among Fmrp HITS-CLIP targets, there were almost 300 microRNAs. Pum1 HITS-CLIP has 60
306 miRNAs, only four of which are not shared with Fmrp; Pum2 HITS-CLIP has no miRNAs that are not
307 shared with either Pum1 or Fmrp (**Figure S6D** and **Table S6**).

308 Because neuronal genes tend to be long (Zylka *et al*, 2015) and RPKM can introduce bias toward
309 longer genes (Mandelboum *et al*, 2019), we wanted to ensure that the targets were actually more highly
310 expressed. Since the published HITS-CLIPs data from other studies were acquired from mice at different
311 ages (but most at 3 weeks of age) and these studies did not typically perform RNAseq in parallel with
312 HITS-CLIP from the same tissue and age, we decided to perform RNAseq from WT mice at 3 weeks of
313 age in triplicate to determine a baseline level of gene expression in mouse brain expressed as DESeq2-
314 normalized counts (Love *et al*, 2014) (see Materials and Methods and **Table S7**). We then normalized
315 RPKM values and repeated the GSEA enrichment analysis. The enrichment between the targets of Pum1
316 and those of Pum2, Ago2, Fmrp, and Rbfox3 was retained even after gene expression normalization
317 (**Figure S6E-G**), with a minimum ES of 0.78, while the maximum score of the negative controls was 0.38
318 (**Figure S6E, F**). The shared targets of Pum1, Pum2, Rbfox3, and Ago2 were even more enriched, with
319 an ES of 0.84 (**Figure S6H**).

320

321 **PUM1 interactors are destabilized in cell lines from PADDAS, but not PRCA, patients**

322 Having identified PUM1 interactors and shared targets, we were now in a position to test our two-
323 pronged hypothesis about how *PUM1* mutations can lead to different diseases. To determine whether
324 either mutation destabilizes PUM1 interactors, we compared their levels in patient-derived cell lines with
325 those in controls. For PADDAS, we compared fibroblasts from one 9-year-old female patient (R1147W;
326 subject 1, or S1) with fibroblasts from three different 9-year-old female healthy controls. For PRCA, we
327 compared lymphoblastoid cells from two female PRCA patients (both with the T1035S mutation; subjects
328 2 and 3, or S2 and S3, 59 and 58 years old, respectively) with lymphoblastoid cells from three different

329 58-year-old female healthy controls (Gennarino *et al.*, 2018). We first measured how much PUM1 we
330 could pull down from the patient-derived cell lines compared to their respective controls. Post-IP did not
331 detect any residual PUM1 from PADDAS or PRCA cell lines, or their controls, confirming that our
332 protocol was able to pull down virtually all of the PUM1 protein from patient-derived cell lines (**Figure**
333 **S7A, B**). IP against PUM1 followed by western blot showed that PADDAS cells had 49%, and PRCA
334 cells 76%, of the amount of PUM1 found in healthy controls (**Figure 6A** and **B**), consistent with our
335 previous report (Gennarino *et al.*, 2018).
336 Co-IP confirmed that PUM1 associates with PUM2, FMRP, AGO2, CNOT1, and MOV10 in patient
337 cell lines (**Figure 6A** and **B**). The mild T1035S variant reduced PUM1 binding to AGO2 by ~21%
338 (**Figure 6B**). The more severe R1147W variant, however, reduced PUM1 association with AGO2,
339 CNOT1, and MOV10 by ~84%, ~59%, and ~90%, respectively (**Figure 6A**). Interaction with FMRP did
340 not appear to be affected. (We could not examine the effect of PUM1 mutations on RBFOX3, which is
341 not expressed in fibroblasts or lymphoblastoid cells.)
342 Western blot analysis revealed that the proteins that lose their association with the R1147W variant
343 undergo reduction in their expression levels (**Figure 6C**). Note that MOV10's association with R1147W
344 was greatly reduced (**Figure 6A**) even though its protein levels were unchanged (**Figure 6C**). AGO2 and
345 CNOT1 levels were unchanged in the PRCA cell line but were ~50% lower in the PADDAS cell line
346 (**Figure 6C**). The mRNA levels of *PUM1*, *AGO2*, *CNOT1*, and *MOV10* did not change (**Figure S7C**),
347 confirming that the reductions in their respective protein levels were due to the loss of interaction with
348 PUM1-R1147W.
349 One limitation of these studies is that we are implicitly comparing different cell types. Since we
350 haven't been able to procure lymphoblasts from PADDAS patients or fibroblasts from PRCA patients, we
351 sought to confirm our findings *in vitro*. We inserted a GST-tag at the N-terminal of *AGO2*, *CNOT1*, and
352 *FMRP* (see Materials and Methods). (AGO2 and CNOT1 were the only proteins whose levels changed in
353 fibroblasts, so FMRP is used here as a control.) We also cloned a Myc-tag polypeptide at the N-terminal
354 of *PUM1*-WT, *PUM1*-R1147W (PADDAS) and *PUM1*-T1035S (PRCA) (see Materials and Methods).
355 We then co-transfected the same amount of Myc-tagged PUM1 proteins with the GST-tagged interactors,
356 followed by western blot to quantify the amount of GST-tagged protein retrieved relative to the quantity
357 of PUM1 proteins pulled down in the IP. GST-AGO2 associated with Myc-PUM1-R1147W 76% less
358 than it did with Myc-PUM1-WT (**Figure 7A**), in alignment with our observations in the PADDAS cell
359 lines (**Figure 6A, B**). We also found ~35% less interaction with CNOT1 (**Figure 7B**) but no decrease in
360 PUM1 association with FMRP (**Figure 7C**), again in accord with our findings in patient-derived cells
361 (**Figure 6A**, **B**).

362 We also examined the effects of the PUM1 mutant on PABPC1, PABPC4, EIF4A3, and EIF4G3
363 (**Figure 1A**), which various studies have indicated interact with each other (Cheng & Gallie, 2007; Gallie,
364 1998; Le *et al*, 1997) and seems to be important for Pumilio activities but not necessarily as its interactors
365 (Goldstrohm *et al.*, 2018; Menon *et al*, 2004). We cloned a GST-tag at the respective N-terminals and
366 performed the experiment as described above. While the R1147W mutation reduced interaction with
367 PABPC1 by roughly 40%, it actually increased interaction with PABPC4 by 350% (**Figure S7D** and **E**).
368 Strikingly, PUM1-R1147W increased interaction with EIF4A3 and EIF4G3 by 1600% to 2760% (**Figure**
369 **S7F** and **G**).
370 These data suggest that the effects of the R1147W mutation, which does not impair PUM1 binding to
371 mRNA (Gennarino *et al.*, 2018), are due to the loss of interactions with RBPs that repress mRNA with a
372 concomitant gain of function with translational initiation proteins.
373
374 **R1147W mutation dramatically destabilizes PUM1**
375 We next tested the PUM1 variants in a protein stability assay. We measured the half-life of the three
376 Myc-tagged PUM1 proteins by separately transfecting 125ng of each. After cycloheximide treatment (T0)
377 to block translation, we quantified the amount of protein at different time points: 30min, 1h, 2h, 4h, and
378 5h, compared to T0 (**Figure S7H**). The half-life of PUM1-WT was roughly 5.5 hours, the half-life of
379 PUM1-T1035S was ~2 hours, and that of PUM1-R1147W slightly less than 1 hour (**Figure S7H**).
380 We also wondered whether the R1147W mutation might be impaired in binding with WT PUM1. It
381 has been thought that Puf proteins do not dimerize (Edwards *et al*, 2001; Zamore *et al*, 1999), but recent
382 work supports this possibility (Qiu *et al*, 2019). We therefore co-transfected each of the Myc-tagged
383 PUM1 variants with the same amount of GST-tagged *PUM1*-WT and used an empty vector as a negative
384 control. First, we confirmed that IP against Myc-PUM1-WT pulled down GST-PUM1-WT. IP against
385 Myc-PUM1-R1147W pulled down 51% of the total GST-PUM1-WT, while the interaction between Myc-
386 PUM1-T1035S and GST-PUM1-WT remained unchanged (**Figure 7D**). The same interaction was
387 observed after RNase treatment, suggesting that mammalian PUM1 dimerizes without RNA (**Figure**
388 **S7I**). These data suggest that the R1147W mutation might exert a dominant-negative effect on wild-type
389 PUM1.
390 The combination of lower protein levels and marked protein instability helps explain why the
391 R1147W phenotype is better represented by the *Pum1* null mice than by the heterozygotes (Gennarino *et*
392 *al.*, 2018).
393
394 **Shared targets are upregulated in PADDAS but not PRCA**

395 We had hypothesized that PRCA would involve dysregulation of PUM1 targets, whereas PADDAS
396 would involve both destabilization of PUM1 interactors and dysregulation of downstream targets of those
397 interactors. We therefore tested the effects of the T1035S and R1147W mutations on validated PUM1-
398 specific targets (Chen *et al*, 2012; Gennarino *et al.*, 2015; Zhang *et al.*, 2017) that are not in the HITS-
399 CLIP data for the other RBPs but are expressed in both fibroblasts and lymphoblasts. PUM1-specific
400 mRNA were dysregulated to very similar extents in PRCA and PADDAS patient cells, with only a few
401 targets being up to 20% more upregulated in PADDAS (**Figure 7E**).
402 We then examined the mRNA levels of all 175 targets shared between PUM1, PUM2, AGO2, FMRP,
403 and RBFOX3 (**Figure 5E** and **Table S5**) in the same PRCA and PADDAS patient cell lines. Of these
404 shared targets, 55 were expressed in both PADDAS fibroblasts and PRCA lymphoblastoid cells. Of these
405 55, 52 shared targets were upregulated in PADDAS but not in PRCA (**Figure 7F**), by an average of two-
406 fold (ranging from a low of 121% for IDS to 347% for TLK1). There was little or no change in most of
407 these targets in PRCA cells, though levels of CALM1, ATP2A2, CREB1, and GNAQ fell by ~40%, and
408 CALM2, TAOK1, and UBE2A by ~20% (**Figure 7F**).
409 These results support our hypothesis that the symptoms observed in PRCA are attributable to the
410 dysregulation of PUM1-specific target genes, while PADDAS involves both protein partner
411 destabilization and dysregulation of the partner proteins' targets.
412
413 **Discussion**
414 Since our initial study describing PUM1-related diseases (Gennarino *et al.*, 2018), we and others have
415 identified additional PADDAS and PRCA patients (Bonnemason-Carrere *et al*, 2019; Gennarino *et al.*,
416 2018; Imaizumi *et al*, 2019; Lai *et al*, 2019). In our sample, R1147W accounts for the majority of
417 PADDAS patients, and T1035S for the majority of PRCA, which supports the value of studying these
418 particular two mutations as causing the most severe and the most mild forms of PUM1-related disease.
419 The question that drove the present study is: why should the 25% drop in PUM1 levels from PRCA to
420 PADDAS produce such different phenotypes, especially when R1147W is not impaired in binding to
421 mRNA? Our data strongly support our hypothesis that the difference is not due to a linear increase in the
422 de-repression of mRNA targets but is rather a function of an additional mechanism coming into play: the
423 destabilization of numerous interactions and the de-repression of their downstream targets. We draw this
424 conclusion from several lines of evidence. First, when Pum1 was reduced by 50% (in heterozygous mice)
425 or 100% (in knockout mice), there were changes in the levels of associated proteins that depended on
426 brain region and sex. Second, we found changes in the levels of these proteins in patient cell lines, despite
427 unchanged mRNA levels. Third, our *in vitro* studies using Myc- and GST-tagged proteins showed that

428 AGO2 and CNOT1 lose their interaction with PUM1-R1147W, which itself binds less to WT PUM1.
429 Fourth, not all interactions were diminished: the responses to R1147W ranged from a loss of 40-70% to a
430 gain of 2760%. Together these data persuade us that a 50% loss of PUM1, whether through
431 heterozygosity or the R1147W mutation, disrupts interactions with native partners and differentiates
432 PADDAS from PRCA.
433
434 *Diseases involving dosage-sensitive proteins*
435 There are other dosage-sensitive proteins that produce different phenotypes depending on their
436 expression level (Tan & Zoghbi, 2019), and our results raise the possibility that interacting complexes
437 may be disrupted once expression falls below a certain threshold. What that threshold might be, exactly,
438 is not clear, but for PUM1 it seems to be somewhere between the 75% of wild-type levels of PUM1 seen
439 in PRCA and the 60% level estimated for the R1139W mutation that produced a milder form of PADDAS
440 (Gennarino et al., 2018). In this context it is worth noting that a recent study found that, below a threshold
441 of ~70% of normal levels of FMRP, there were steep decreases in IQ for each further decrement in FMRP
442 levels, even as small as 5-10% (Kim *et al*, 2019). The amount of loss that can be sustained for a given
443 protein would likely depend on its usual quantities, and it is possible that for some proteins, the difference
444 in phenotype between greater and lesser abundance may indeed reflect a linear progression from mild to
445 severe. For example, a mutation in *MECP2* that reduces the protein levels by only 16% causes a mild
446 form of Rett syndrome: the child developed normally until the age of two years, then regressed, lost
447 acquired language and manual skills, and developed hand stereotypies (Takeguchi *et al*, 2020). She
448 eventually regained the ability to repeat words in an echolalic fashion and never developed seizures, but
449 the phenotype was clearly Rett syndrome. The relationship between protein levels and disease features in
450 MeCP2-related disorders may be more linear because this protein is so extraordinarily abundant
451 (Sandweiss *et al*, 2020). Similarly, in proteopathies such as Alzheimer's or Parkinson's disease, genetic
452 duplications of *APP* or *SNCA* cause earlier onset of what is recognizably the same disease (Chartier-
453 Harlin *et al*, 2004; Rovelet-Lecrux *et al*, 2006).
454 In contrast, there are diseases in which the phenotypes do not simply range from mild to severe
455 versions of the same symptoms, but seem to take on a different character. The polyglutamine diseases,
456 such as Huntington's disease and the spinocerebellar ataxias, come to mind, perhaps because it was
457 through studying spinocerebellar ataxia type 1 (SCA1), that PUM1's role in neurological function was
458 discovered (Gennarino *et al.*, 2015). In the polyglutaminopathies, the disease-causing protein bears an
459 abnormally expanded CAG tract that tends to expand upon intergenerational transmission. Although the
460 range of normal and pathogenic repeat tract lengths differs from one polyglutamine disease to another,

461 larger expansions are more unstable, cause earlier onset, and affect far more tissues than smaller
462 expansions (Orr & Zoghbi, 2007). For example, adult-onset SCA7 presents as ataxia, but infantile SCA7
463 affects the entire nervous system, the heart, and the kidneys, and leads to death by two years of age (Bah
464 *et al*, 2020). Another example is Huntington's disease, where the juvenile form frequently lacks the
465 classic chorea yet produces seizures, which are not a feature of the adult-onset disease; brain
466 morphometry is also quite different in adult- and juvenile-onset cases (Tereshchenko *et al*, 2019). In this
467 family of diseases, therefore, the mechanism is technically the same—repeat expansion—but different
468 tissues have different thresholds for the CAG repeats. In the case of PUM1-related disease, it seems that
469 an additional mechanism comes into play for the more severe phenotypes, beyond upregulation of mRNA
470 targets. Interestingly, FMRP, which harbors a dynamic CGG repeat, is also associated with very different
471 diseases, through two different mechanisms. Very large expansions silence the gene and produce Fragile
472 X syndrome, whereas premutations are thought to cause the adult-onset Fragile-X-associated
473 tremor/ataxia syndrome through RNA toxicity (Salcedo-Arellano *et al*, 2020).
474
475 *Implications of the interactome*
476 It has never been clear how the various modes of action attributed to PUM1 or other RBPs relate to
477 one another, in large part because studies typically focus on one protein or pathway at a time. Our data
478 suggest that the three mechanisms of repression that have been proposed for PUM1 may be coordinated in
479 neurons, insofar as PUM1, PUM2, FMRP, AGO2, MOV10, CNOT1 and RBFOX3 (and related proteins
480 in specific brain regions) either interact or are so close to each other within the ribonucleosome that the
481 loss of Pum1 or RNA can change the composition of the complexes that are identified by co-IP, in ways
482 that are specific to brain region and sex. In this context it is worth noting that a very recent study found
483 alternative splicing is altered in hippocampal slices from Fmrp-deficient mice; this observation was
484 attributed to changes in H3K36me3 levels (Shah *et al*, 2020). Our data suggest that FMRP has an even
485 closer relationship with the RBFOX protein family and alternative splicing machinery than suspected.
486 Indeed, recent work has provided tantalizing glimpses of close interactions among various kinds of RNA
487 metabolism. For example, members of the RBFOX family of proteins may, depending on their interactors
488 (and perhaps cell type, sex, age, and species), be involved in microRNA processing in the nucleus and
489 translation in the cytoplasm (Conboy, 2017). The FMRP/MOV10 complex appears to be involved in
490 regulating translation through miRNA, with evidence that this role may change according to cell type
491 (Kenny *et al.*, 2020). Another study used quantitative mass spec to examine how Fmrp expression levels
492 change with age in the wild-type rat dentate gyrus, and found differences in the levels of myriad proteins;
493 among the 153 proteins with the most significant changes in levels were Pum1, Pum2 and Papbc1

494 (Smidak *et al*, 2017). The region-, sex-, and age-specificity of certain interactions indicates that
495 unraveling RBP interactomes *in vivo* will require considerable finesse.
496 Although we did not pursue the entire interactome here, future studies investigating interactions
497 between PUM1 and members of the mTOR pathway and anaphase-promoting complex should be very
498 fruitful. As we were preparing this work, a new study demonstrated that mTORC1 is involved in
499 postsynaptic responses in hippocampal glutamatergic neurons, whereas mTORC2 modulates presynaptic
500 release (McCabe *et al*, 2020). Given the importance of proteostasis at the synapse—and its failure in
501 many neurological diseases (Zoghbi & Bear, 2012)—the notion that different protein-regulating activities
502 might be coordinated is intuitively appealing.
503 There is still much to be understood about how PUM1 works, and where and how the various
504 RNA metabolic machineries come into contact. The fact that several associations we tested are RNA-
505 independent suggests that certain complexes may form prior to binding mRNA. Could different pools of
506 PUM1 form different complexes that determine whether and where a target is bound? Do the subtle
507 differences between brain regions in the choice of interacting partners from the same pathways influence
508 target choice, activity, or both? Given that mRNA is much larger than proteins, is the quantity of these
509 RBPs so great that they coat the RNA? What other proteins may be involved in 'handing off' an mRNA
510 from one pathway to another? Although we began this study to better understand Pum1 functions in
511 neurons, and thus have been rather Pum1-centric, it is by no means certain that Pum1 is the only protein
512 that links these different molecular machineries. It may be simply the first of several missing links that we
513 didn't realize were missing. Creating RBP interactomes should lead to a more complex yet realistic
514 picture of RBP roles in neuronal function and in neurological disease.
515
516 **Acknowledgments**
517 We thank the patients, their families, and their clinical teams for participating in our study, and the
518 anonymous reviewers for helpful suggestions. We thank Mingyu Cao for help with statistical analyses
519 and U.N. Wasko for starting the cloning procedure with Myc and GST tag sequences *in vitro*. We also
520 thank G. Struhl, V. Ambros, T. Duchaine, G. Karsenty, H. Zoghbi, M. Jovanovic, Y. Giardina, and
521 members of the Gennarino laboratory for helpful discussions and support. This work was supported by
522 the National Institute of Neurological Disorders and Stroke (NINDS; R01NS109858 to V.A.G.); the
523 National Ataxia Foundation/Young Investigator Research Grant (V.A.G.); the Brain & Behavior Research
524 Foundation Young Investigator Award; and the Paul A. Marks Scholar Program, Columbia University
525 Vagelos College of Physicians and Surgeons. This project was also supported by the Genomic and RNA
526 Profiling Core at Baylor College of Medicine and the Bioinformatics Core at the Jan and Dan Duncan

527 Neurological Research Institute. The authors declare no competing interests.
528
529 **Author Contributions**
530 S.B. designed and performed molecular experiments, analyzed and interpreted the data, and drafted the
531 manuscript. N.D.P. performed the qPCR experiments, *in vitro* immunoprecipitation assays, analyzed the
532 data, and edited the manuscript. A.C. performed all the brain region dissections in mice, performed the
533 qPCR experiments and maintained the *Pum1* mutant mouse colony. M.C. performed the cloning
534 experiments. V.L.B. interpreted data and wrote the manuscript. P.P and R.K.S. performed mass
535 spectrometry and helped analyze the data. V.A.G. conceived the study, analyzed and interpreted the data,
536 performed molecular experiments, and wrote the manuscript.
537
538 **Declaration of Interests**
539 The authors declare not competing interests
540
541 **Main Figure Titles and Legends**
542 **Figure 1. A brain-specific Pum1 interactome.** (**A**) Network of putative Pum1 interactors in 10-week-
543 old mouse brain (circles connected to Pum1 by gray lines). Interactions between interactors (purple lines)
544 inferred by g:GOSt from Corum and the Human Protein Atlas (see Materials and Methods). The proteins
545 in each of the 22 clusters are listed to the right. (**B**) Bubble plots show the top categories from gene
546 ontology analyses of Pum1 interactors from whole brain, hippocampus, cortex, and cerebellum. Only the
547 categories with fold enrichment >1.5 and FDR<0.05 are shown; not all are labeled because of space
548 limitations (see **Table S2**).
549
550 **Figure 2. Validation of Pum1 associations with post-transcriptional RNA-binding proteins in mouse**
551 **brain.** (**A**) Representative western blot of proteins pulled down by IP against Pum1 compared to IgG
552 from wild-type mice brain without (*left*) and with (*right*) RNase treatment. In this panel, after IP-Pum1,
553 we immunoblotted for Pum1 (positive control), Pum2, Fmrp, Ago2, Rbfox3, Cnot1, and Mov10. (See
554 Materials and Methods.) (**B**) Representative western blot of the reciprocal IPs against Pum2, Fmrp, Ago2,
555 Rbfox3, Cnot1 or Mov10. Each IP was immunoblotted against Pum1 and the putative interactor. (**C**)
556 Representative western blots of the same proteins validated in panels **A** and **B** after IP against PUM1 with
557 or without RNase treatment from HEK293T cell lines. In panels **A** through **C**, IP against IgG was used as
558 a negative control and Input (1% from the initial protein lysate) as a loading control. The numbers on the
559 right are the respective molecular weights expressed in kilodaltons (kDa). All the experiments were

560 repeated at least six times. All mice were sacrificed at 10 weeks of age.

561

562 **Figure 3. Effects of Pum1 loss on interactions among the six RNA-binding proteins.** Representative
563 western blot of the proteins pulled down by (**A**) Pum2, (**B**) Fmrp, (**C**) Rbfox3, (**D**) Mov10, (**E**) Ago2, and
564 (**F**) Cnot1 from WT and *Pum1*$^{-/-}$ mouse brain at 10 weeks of age. IP against IgG was used as negative
565 control, and Input (1% from the initial protein lysate) as loading control. Molecular weights to the right
566 are expressed in kilodaltons (kDa). All the experiments were repeated at least four times. Since Rbfox3
567 and Mov10 interactions with Pum1 are RNA-dependent we did not perform IP from *Pum1*$^{-/-}$ mouse brain.

568

569 **Figure 4. Pum1 interactors and the microRNA machinery show brain region- and sex-specific**
570 **responses to Pum1 loss.** Representative western blots of Pum1, Pum2, Fmrp, Ago2, Rbfox3, Cnot1, and
571 Mov10 in (**A**) cerebellum, (**B**) hippocampus, and (**C**) cortex in both male (left panel) and female (right
572 panel) WT, *Pum1*$^{+/-}$, and *Pum1*$^{-/-}$ mice. The same number of males and females at 10 weeks of age was
573 used for a total of at least 18 mice per genotype. Graphs below show quantification for each protein by
574 brain region, sex, and genotype. All data were normalized to Gapdh protein levels. All experiments were
575 performed at least 9 times per genotype from mice at 10 weeks of age (data represent mean ± SEM). *P*
576 values were calculated by two-tailed Student's t test. *$p < 0.05$, **$p < 0.01$, ***$p < 0.001$. See **Figure**
577 **S5A** for mRNA quantification for each interactor, brain region, and sex. P1 indicates Pumilio1. (**D**)
578 Heatmap showing 166 microRNAs from mouse cerebellum in *Pum1*$^{-/-}$ male and female mice at 10 weeks
579 of age that were dysregulated (fold change -3 to +3) relative to wild-type cerebellum. Three cerebella per
580 genotype and sex were analyzed (see **Table S3** for the microRNA names and fold changes). (**E**) Heatmap
581 showing mRNA quantification by qPCR for 49 targets co-bound by a minimum of eight dysregulated
582 miRNAs (>20% change) from panel **D**. Three cerebella per genotype and sex were analyzed. Statistical
583 significance and magnitude of dysregulation are illustrated for both male and female in **Figure S5B**.

584

585 **Figure 5. Pum1 and its RNA-binding protein interactors share many neuronal mRNA targets.** (**A**)
586 Enrichment plots generated by Gene Set Enrichment Analysis (GSEA) of Pum1, Pum2, Rbfox3, and
587 Ago2 HITS-CLIP targets plotted again Fmrp HITS-CLIP data ranked by RPKM. Pum1, Pum2, Rbfox3,
588 and Ago2 targets are enriched at the top 10th percentile of the Fmrp targets with FDR=0. (**B**) GSEA
589 analysis scores of HITS-CLIP data from each negative control (Apc, Nova, Ptpb2, and Mbnl2) plotted
590 against Fmrp HITS-CLIP data ranked by RPKM. The negative controls have a maximum enrichment
591 score of 0.36 for Apc ranking at the top 44.7% with FDR=1. (**C**) GSEA analysis scores of Pum1, Pum2,
592 Rbfox3, and Ago2 HITS-CLIP data plotted against Fmrp HITS-CLIP data divided into 10-percentile bins

593 and ranked by RPKM shows the shared targets are among the top percentiles of targets for each protein.
594 (**D**) GSEA analysis scores of the HITS-CLIP data for Fmrp, Pum2, Ago2, Rbfox3 and four negative
595 controls (Apc, Nova, Ptpb2, and Mbnl2) against Pum1 HITS-CLIP data ranked by RPKM. The targets of
596 Fmrp, Ago2, Pum2, and Rbfox3 are enriched at the top 5th to 18th percentile of Pum1 targets. (**E**) GSEA
597 analysis of the shared targets between Pum1, Pum2, Ago2, and Rbfox3 against Fmrp showing that they
598 are enriched in the top 5th percentile of Fmrp targets ranked by RPKM. (**F**) Pum1, Pum2, Ago2, and
599 Rbfox3 shared targets plotted against Fmrp HITS-CLIP targets ranked by RPKM and divided into 10-
600 percentile bins shows that all of their respective targets are enriched at the top 10th percentile of the Fmrp
601 targets ranked by RPKM. (**G**) GSEA analysis scores of the targets shared by Pum1, Pum2, Ago2, and
602 Rbfox3 and the four negative controls (Apc, Nova, Ptpb2, and Mbnl2) plotted against Fmrp. At best the
603 negative controls are enriched at the top 40% with a maximum ES of 0.41. For all the GSEA analyses, the
604 False Discovery Rate (FDR) was provided by GSEA: **FDR<0.05 and ***FDR<0.01. ES=Enrichment
605 score (blue line). Note that lowest rank at max percentage indicates stronger targets in the rank (see
606 Materials and Methods).
607
608 **Figure 6. The R1147W mutation, but not T1035S, destabilizes PUM1 interactors.** (**A**) IP against
609 PUM1 from PADDAS (R1147W) patient (Subject 1 or S1)-derived fibroblasts confirms the interactions
610 between PUM1 (used here as a positive control), and PUM2, FMRP, AGO2, CNOT1, and MOV10.
611 *Bottom panel*: protein quantification shows loss of interaction between PUM1-R1147W and AGO2,
612 CNOT1 and MOV10 compared to three age- and sex- matched control fibroblasts. Input (1%) was used
613 as a loading control and IP against IgG was used as a negative control. (**B**) IP against PUM1 from two
614 PRCA (T1035S) patient (S2 and S3)-derived lymphoblastoid cell lines confirm the interaction between
615 PUM1 (used here as positive control), and PUM2, FMRP, AGO2, CNOT1, and MOV10. *Bottom panel*:
616 protein quantification shows a slight decrease in interactions with FMRP and AGO2, and a slight increase
617 with CNOT1 and MOV10, compared to age- and sex- matched lymphoblastoid controls. Input (1%) was
618 used as a loading control and IP against IgG was used as a negative control. In **A** and **B**, the amount of
619 protein pulled down compared to IP-PUM1 was quantified as follows: $[IP^{X}/(Input^{X}/GAPDH^{X})]/$
620 $[IP^{PUM1}/(Input^{PUM1}/GAPDH^{PUM1})]$, where X is the protein of interest. (**C**) Representative western blots
621 (*left panels*) and relative quantification (*bar graphs to the right*) of protein levels for PUM1, PUM2,
622 FMRP, AGO2, CNOT1, and MOV10 in PADDAS patient-derived fibroblasts and PRCA patient-derived
623 lymphoblastoid cells compared to their respective age- and sex- matched fibroblast (for PADDAS
624 patients) and lymphoblastoid (for PRCA patients) controls. Data were normalized to Gapdh protein
625 levels. From **A** to **C**, all the experiments were performed at least six times. Data represent mean ± SEM. P

values were calculated by two-tailed Student's t test. *$p < 0.05$, **$p < 0.01$, ***$p < 0.001$.

Figure 7. RBP complexes with PUM1 R1147W are destabilized *in vitro* and shared neuronal targets are upregulated only in PADDAS. (**A**-**D**) Representative western blots and relative IP quantification (*bar graphs*) of IP against Myc-PUM1-WT, Myc-PUM1-T1035S (PRCA), or Myc-PUM1-R1147W (PADDAS) followed by immunoblotting for: (**A**) GST-AGO2, (**B**) GST-CNOT1, (**C**) GST-FMRP, and (**D**) GST-PUM1-WT. Myc- and GST-tagged proteins were co-transfected in HEK293T cells in equal quantities (250ng each). The molecular weights were expressed in kilodaltons (kDa). The amount of protein pulled down compared to IP-PUM1 was quantified as $[IP^{X}/(Input^{X}/GAPDH^{X})]/[IP^{PUM1}/(Input^{PUM1}/GAPDH^{PUM1})]$, where X is the protein of interest. (**E**) qPCR analysis of validated PUM1-specific targets from PADDAS patient-derived fibroblasts (S1, blue bars) compared to three age- and sex-matched fibroblast control cell lines, and PRCA patient-derived lymphoblastoid cell lines (S2 and S3, orange bars) compared to the three age- and sex-matched lymphoblastoid control cell lines. (**F**) mRNA level quantification of PUM1 neuronal targets in common with FMRP, PUM2, AGO2, and RBFOX3 (**Figure 5E** and **Table S5**) in fibroblasts from subject 1 (PADDAS patient, R1147W) compared to the three age- and sex-matched control fibroblast lines (blue bars), and in lymphoblastoid cells from subjects 2 and 3 (PRCA patients, T1035S) compared to the three age- and sex-matched control lymphoblastoid cell lines (orange bars). For **E** and **F**, all data were normalized to *GAPDH* mRNA levels and experiments performed at least three times. Only genes expressed in both fibroblasts and lymphoblasts are represented here for a total of 10 for panel **E** and 55 for panel **F**. Data represent mean ± SEM. P values were calculated by two-tailed Student's t test. *$p < 0.05$, **$p < 0.01$, ***$p < 0.001$.

Supplemental Figure Legends

Figure S1. Immunoprecipitation (IP) antibody specificity against Pum1 from mouse brain and Pum1 interactor validation. (**A**) Pre-IP, IP, and post-IP against Pum1 and IgG from wild-type mouse brain show the specificity of the antibody used against Pum1. Pre-IP represents 1% from the initial protein lysate as loading control while 10% of the protein lysate after IP-Pum1 was loaded as post-IP. The numbers on the right show molecular weight in kilodaltons (kDa). (**B**) Principal component analysis (PCA) of IP-Pum1 followed by mass spectrometry (MS) in WT adult mouse brains compared with IP against IgG; each dot represents two combined samples for a total of 6 samples processed by mass spectrometry. (**C**) Representative western blot of Rptor, Cad, Anapc1 and Fzr1 proteins pulled down by IP against Pum1 (used here as positive control) from WT mice. (**D**) Representative western blot of the reciprocal co-IPs against Anapc1, Fzr1, Rptor, and Cad. Each co-IP was immunoblotted against Pum1

659 and the pulled down protein used here as a reference protein to confirm the respective protein-protein
660 interaction. For **C** and **D**, IP against IgG was used as negative control, and Input (1% from the initial
661 protein lysate) as loading control. Molecular weights are expressed in kilodaltons (kDa) to the right. All
662 the experiments were repeated at least four times. All mice were sacrificed at 10 weeks of age with an
663 equal number or male and female.
664
665 **Figure S2. Pum1 interactors differ by brain region.** (**A**) Principal component analysis (PCA) of IP-
666 Pum1 followed by mass spectrometry (MS) in cortex, hippocampus, and cerebellum from WT mice. IP
667 against IgG was used as negative control. Each dot represents a total of 3 samples processed by MS for
668 each brain region. (**B**) Pum1 interactome from cerebellum, hippocampus, cortex and the rest of the brain
669 (i.e., excluding those three regions) showing all Pum1 putative interactors with a fold change > 1.5 (see
670 also **Table S1**), for a total of 1,500 proteins. Node colors represent different brain regions or the overlap
671 between two or more brain regions as noted. (**C**) After IP against Pum1 we immunoblotted for Pum1
672 (positive control), Anapc1, Cnot1 and Pum2. While Cnot1 and Anapc1 can be pulled down from all three
673 brain regions, Pum2 can only be pulled down from cortex. For **A-C** we combined cerebellar and cortical
674 tissues from eight wild-type mice (4 male and 4 female) for a total of 24 mice in triplicate for cerebellum
675 and cortex, while for hippocampus we combined tissues from ten wild-type mice (5 female and 5 male)
676 for a total of 30 mice in triplicate. All mice were 10 weeks of age. IP against IgG was used as negative
677 control. Molecular protein weights are expressed in kilodaltons (kDa). (**D-F**) The three most enriched
678 protein complexes among the Pum1 interactors for each brain region are shown in (**D**) for the anaphase
679 promoting complex/cyclosome (APC/C); (**E**) for the mTOR pathway; (**F**) for RNA-silencing (RISC),
680 CCR4-NOT, translation initiation and polyA binding. Edge colors (**D**, **E**, and **F**) represent a specific brain
681 region: red for cortex, green for cerebellum, blue for hippocampus, and gray for proteins in common
682 between two or more brain regions. (**G**) Western blot analysis at 10 weeks of age to evaluate Pum2
683 expression levels in eight different brain regions as well as whole brain. Pum2 is highly expressed in
684 olfactory bulbs and amygdala, and expressed at similar levels in hippocampus, cerebellum, and cortex.
685 HP: hippocampus; CB: cerebellum; CX: cortex; MB: midbrain; OB: olfactory bulbs; AM: amygdala; SN:
686 substantia nigra pars compacta; BS: brain stem; WB: whole brain.
687
688 **Figure S3. Immunoprecipitation (IP) against Pum1 and its interactors in wild-type and *Pum1*$^{-/-}$ mice**
689 **with and without RNase treatment.** (**A**) IP against Pum1 in *Pum1*$^{-/-}$ mouse demonstrates the complete
690 absence of Pum1 and thus the specificity of the anti-Pum1 antibody. (**B-G**) Representative western blot of
691 the proteins pulled down by (**B**) Pum2, (**C**) Fmrp, (**D**) Ago2, (**E**) Cnot1, (**F**) Mov10, and (**G**) Rbfox3 from

692 wild-type (WT, *left panel*) and *Pum1*$^{-/-}$ (*right panel*) mouse brain without (*left panel*) and with (*right*
693 *panel*) RNase treatment. IP against IgG was used as negative control, and Input (1% from the initial
694 protein lysate) as loading control. Molecular weights at the right are in kilodaltons (kDa). All the
695 experiments were repeated at least four times. IP against IgG was used as negative control, and Input (1%
696 from the initial protein lysate) as loading control. Equal numbers of male and female mice were sacrificed
697 at 10 weeks of age.
698
699 **Figure S4. Protein and mRNA quantification from whole brain in WT, *Pum1*$^{+/-}$ and *Pum1*$^{-/-}$ mice.**
700 (**A**) Representative western blot with relative quantifications of Pum1, Pum2, Fmrp, Ago2, Rbfox3,
701 Cnot1, and Mov10 from the whole brain in WT, *Pum1*$^{+/-}$ and *Pum1*$^{-/-}$ mice. All data were normalized to
702 Gapdh protein levels. The numbers on the right are the respective molecular weights expressed in
703 kilodaltons (kDa). (**B**) mRNA level quantification by qPCR of *Pum1*, *Pum2*, *Fmrp*, *Ago2*, *Rbfox3*, *Cnot1*,
704 and *Mov10* from whole brain in WT, *Pum1*$^{+/-}$ and *Pum1*$^{-/-}$ mice. Again, all data were normalized to *Gapdh*
705 mRNA levels. All the experiments were conducted with equal number of male (at least 6 per genotype)
706 and female (at least 6 per genotype) mice at 10 weeks of age, for a total of at least 12 mice per genotype,
707 performed at least six times per genotype (data represent mean ± SEM). The *p* values were calculated by
708 the Student's t test. *$p < 0.05$, **$p < 0.01$, ***$p < 0.001$.
709
710 **Figure S5. mRNA quantification of Pum1 interactors by brain region and sex and the 49 targets co-**
711 **bound by at least eight dysregulated miRNAs in mouse cerebellum.** (**A**) mRNA levels in cerebellum,
712 hippocampus, and cortex in male and female for all the validated Pum1 interactors. The same number of
713 mice were used here as in **Figure 4A-C** for a total of at least 9 mice per genotype and sex at 10 weeks of
714 age. All data were normalized to *Gapdh* mRNA levels. All the experiments were performed at least six
715 times (data represent mean ± SEM). (**B**) qPCR in cerebellum of male (*left*) and female (*right*) mice at 10
716 weeks of age for the 49 targets co-bound by at least eight dysregulated miRNAs (with minimum 20%
717 change in expression) from **Figure 4E** and **Table S4**. All the experiments were performed in triplicate for
718 three different biological replicates for both male and female (data represent mean ± SEM). The *p* values
719 were calculated by two-tailed Student's t test. *$p < 0.05$, **$p < 0.01$, ***$p < 0.001$.
720
721 **Figure S6. Pum1, Pum2, Ago2, Fmrp, and Rbfox3 share a number of targets in the mouse brain.**
722 (**A**) Gene Set Enrichment Analysis (GSEA) of Pum1 HITS-CLIP data plotted against HITS-CLIP data
723 from the negative controls (RNA binding proteins that did not show up in the Pum1 interactome: Ptpb2,
724 Nova, Apc, and Mbnl2) reveals no significant enrichment. (**B-C**) Gene ontology analysis of the HITS-

725 CLIP targets shared between Pum1, Pum2, Fmrp, Ago2, and Rbfox3 reveals enrichment for certain (**B**)
726 biological functions and (**C**) cellular localization. Only categories with FDR<0.05 and fold enrichment >
727 5 were plotted in **B** and **C**. (**D**) Venn diagram of miRNAs identified by Pum1, and Pum2 shows almost
728 100% overlap with the miRNAs pulled down by Fmrp HITS-CLIP. (**E**) GSEA of HITS-CLIP data
729 normalized against gene expression in mouse brain at 3 weeks of age (see Materials and Methods) of
730 Pum1, Pum2, Rbfox3, and Ago2 against Fmrp HITS-CLIP data ranked by normalized RPKM. (**F**) GSEA
731 of HITS-CLIP data normalized against gene expression in mouse brain at 3 weeks of age (see Materials
732 and Methods) of Mbnl2, Apc, Nova, and Ptpb2 plotted against Fmrp HITS-CLIP data ranked by
733 normalized RPKM. Mbnl2, Ptpb2, Apc, and Nova were used as negative controls. (**G**) Fmrp, Pum2,
734 Ago2, Rbfox3 shared targets, and targets of the four negative controls, plotted against Pum1 HITS-CLIP
735 data ranked by normalized RPKM. (**H**) Pum1, Pum2, Ago2, Rbfox3 shared targets plotted against Fmrp
736 HITS-CLIP data ranked by normalized RPKM. For all GSEA analyses the False Discovery Rate (FDR)
737 was provided by GSEA, ***FDR < 0.01. ES=Enrichment score (blue line). Note that lowest rank at max
738 percentage ES indicates stronger targets in the rank.
739
740 **Figure S7. PUM1 validation experiments in patient-derived cells and in vitro** (**A**-**B**) Pre-IP, IP, and
741 post-IP against PUM1 and IgG from (**A**) PADDAS fibroblasts and (**B**) PRCA lymphoblastoid cells. In
742 both cell lines we were able to pull down 100% of PUM1. Pre-IP represents 1% from the initial protein
743 lysate as loading control, while 10% of the protein lysate was loaded as post-IP. Molecular
744 weights provided at right in kilodaltons (kDa). (**C**) mRNA level quantification for all of the
745 immunoblotted proteins in **Figure 6C** in PADDAS and PRCA patient-derived cell lines compared to their
746 respective age-, sex-, and cell-type-matched controls. All data were normalized to *GAPDH* mRNA levels,
747 and experiments performed at least six times. Data represent mean ± SEM. (**D**-**G**) Representative western
748 blots (upper panel) and relative IP quantification (bottom panel) of IP against Myc-PUM1-WT, Myc-
749 PUM1-T1035S (PRCA), or Myc-PUM1-R1147W (PADDAS) followed by immunoblotting for: (**D**) GST-
750 PABPC1, (**E**) GST-PABPC4, (**F**) GST-EIF4A3, and (**G**) GST-EIF4G3. Myc- and GST-tagged proteins
751 were co-transfected in HEK293T cells in equal quantities (250ng each). The molecular weights were
752 expressed in kilodaltons (kDa). The amount of protein pulled down compared to IP-PUM1 was quantified
753 as $[IP^{X}/(Input^{X}/GAPDH^{X})]/ [IP^{PUM1}/(Input^{PUM1}/GAPDH^{PUM1})]$, where X is the protein of interest.
754 (**H**) PUM1 half-life in HEK293T at different time points, from zero (cycloheximide treatment) to 5h total
755 upon transfection of Myc-PUM1-WT, Myc-PUM1-T1035S, or Myc-PUM1-R1147W. The half-life of the
756 R1147W mutant is significantly shorter than that of WT and T1035S. All data were normalized to
757 GAPDH and compared to time zero. The experiments were performed at least four times and the data

758 represent mean ± SEM. The *p* values were calculated by two-tailed Student's t test. ***p* < 0.01, ***p <
759 0.001. (**I**) Representative western blots of IP with RNase treatment against Myc-PUM1-WT, Myc-PUM1-
760 T1035S (PRCA), or Myc-PUM1-R1147W (PADDAS) followed by immunoblotting to
761 test binding between PUM1 proteins without the RNA. The numbers on the right are the respective
762 molecular weights expressed in kilodaltons (kDa).

763 **Supplemental Tables and Legends**

764 **Table S1, to generate Figure 1A, S1 and S2. Pum1 mass spectrometry results from whole brain and**
765 **three separate brain regions in 10-week-old mice.** All the proteins have an FDR < 0.05, and only
766 proteins with a Ratio LFQ-Pum1-WT/LFQ-IgG-WT > 1.5 are reported here.
767

768 **Table S2, to generate Figure 1B. Gene Ontology analysis of Pum1 mass spectrometry from whole**
769 **brain and the three brain regions.** Only categories with fold enrichment of >1.5 and FDR<0.05 are
770 shown.
771

772 **Table S3, to generate Figure 4D. MicroRNA names and sequences with log2 fold change as**
773 **represented in Figure 4D. PC = Predicted Candidate.**
774

775 **Table S4, to generate Figure 4E and S5B. Predicted target genes for all the differentially expressed**
776 **miRNA (with at least 25% change) in cerebellum of male and female in wild-type and *Pum1*$^{-/-}$ mice**
777 **at 10 weeks of age.** The target genes tested have at least 8 co-bound miRNAs.
778

779 **Table S5, to generate Figure 5, S6, and 7F. HITS-CLIP targets common to Pum1, Pum2, Ago2,**
780 **Rbfox3, and Fmrp.**
781

782 **Table S6, to generate Figure S6D. microRNAs that overlap between Pum1, Pum2, and Fmrp HITS-**
783 **CLIP data.**
784

785 **Table S7, to generate Figure S6E-H. RNAseq in mouse brain at 3 weeks of age.**
786

787 **Table S8. All primer sequences used in this study**
788

789 **Resource Availability**

790 **Lead Contact**

791 Further information and requests for resources and reagents should be directed to and will be fulfilled by
792 Vincenzo A. Gennarino (vag2138@cumc.columbia.edu).

793

794 **Materials Availability**

795 All unique reagents, cell lines and mouse models used in this manuscript are available upon request
796 without restrictions.

797

798 **Materials and Methods**

799 **Ethical statement and mouse strains.** All animal procedures were approved by the Institutional Animal
800 Care and Use Committee at Columbia University, New York under the protocol AC-AAAU8490. Mice
801 were maintained on a 12-hr light, 12-hr dark cycle with regular chow and water ad libitum. Pum1 knock-
802 out mice were generated as previously described (Chen *et al.*, 2012). C57BL/6J wild-type mice were
803 purchased from Jackson Laboratory and maintained as described above. For brain dissection, mice were
804 anesthetized with isoflurane, and the brain rapidly removed from the skull and lysed in the appropriate
805 buffer according to the experiment (see Materials and Methods Details).

806

807 **HEK293T cell culture and maintenance.** Human embryonic kidney immortalized 293T (HEK293T)
808 cells were grown in DMEM (GenDepot, #CM002-320) supplemented with 10% of heat-inactivated fetal
809 bovine serum (FBS [GenDepot, #F0901-050) and 1% penicillin/streptomycin (GenDepot, #CA005-010).
810 All cells were incubated at 37 °C in a humidified chamber supplemented with 5% CO_2. HEK293T cells
811 were later processed according to the needs of specific experiments (described below).

812

813 **Patient-derived cell lines: fibroblasts and lymphoblasts.** PADDAS and PRCA patient cell lines are the
814 same as those reported previously (Gennarino *et al.*, 2018). The consent form for each subject specifically
815 allows for sharing of medical information and physical exam findings; the sharing of cell lines from the
816 PADDAS and PRCA subjects and the controls was approved under the Baylor College of Medicine IRB
817 H-34578 and the Columbia University Medical Center IRB-AAAS7401 (Y01M00).

818 Primary fibroblasts from the *PUM1* PADDAS patient and the age- and sex-matched controls were
819 generated as previously described (Gennarino *et al.*, 2018). Briefly, cells were isolated from skin biopsies
820 taken from the patient or age-matched controls using standard methodology (Barch and Association of
821 Cytogenetic Technology, 1991) and placed in a transport medium (Ham's F10, Thermo Scientific,
822 #11550043). The skin specimen was later removed from the transport medium using a sterile technique

823 (in a Class II biohazard cabinet) and transferred to a sterile Petri dish where it was cut into small pieces (<
824 0.5 mm) using sterile scalpel blades. These pieces were transferred to the lower surface of a 25 cm^2
825 culture flask (6-8 pieces per flask) which had been pre-moistened with 1-2 mL of AmnioMAX Complete
826 Medium (Thermo Scientific, #11269016) supplemented with 1% penicillin/streptomycin (GenDepot,
827 #CA005-010). Cell cultures were maintained at 37 °C in a humidified incubator supplemented with 5%
828 CO_2. When cell growth was observed around the edges of the tissue, usually 3 to 5 days later, 2 to 3 mL
829 of AmnioMAX Complete Medium were added. Once growth was established and the tissue was anchored
830 to the flask, another 8 mL of AmnioMAX Complete Medium was added. Thereafter, the medium was
831 renewed every 3 to 4 days until ready for sub-culturing.
832 Lymphoblastoid cells from *PUM1* PRCA patients and the age- and sex-matched controls were
833 generated as previously described (Gennarino *et al.*, 2018). Briefly, lymphoblastoid suspension cell
834 cultures were grown in RPMI 1640 medium (Invitrogen, #11875093) supplemented with 10% heat-
835 inactivated fetal bovine serum (Atlanta Biological, Flowery Branch, #S11195H) and 1%
836 penicillin/streptomycin (GenDepot, #CA005-010). Cell cultures were maintained at 37°C in a humidified
837 incubator supplemented with 5% CO_2. Medium was renewed every 2 to 3 days.
838
839 **Immunoprecipitation experiments using mouse brain tissue.** Mouse brain tissues were gathered from
840 an equal number of 10-week-old male and female mice as follows: whole brains from two mice;
841 hippocampi from ten mice; cerebral cortices from eight mice; and cerebella from eight mice. Each
842 grouping is considered one sample for one experiment. Samples were processed with a dounce
843 homogenizer using a lysis buffer consisting of 200mM $NaCl_2$, 100mM $NaPO_4$, 20mM Hepes pH 7.4, 1%
844 Triton X (which should disrupt all but the strongest protein-protein interactions) and complemented by
845 1X of Xpert Protease and 1X of Phosphatase Inhibitor Cocktail Solutions (GenDepot, #P3100-100,
846 #P3200-020). Following homogenization, the samples were placed on ice for 15 minutes then centrifuged
847 at 14,800 rpm at 4°C for 25 minutes to remove the debris from the supernatant. The supernatant was then
848 moved to 1.5 ml tubes (Beckman microfuge tube #357448) and spun down in a Beckman ultra-centrifuge
849 (Optima Max XP) at 4°C for 25 minutes at 44,000 rpm. 10% of the protein lysate was stored as input and
850 only 1% was loaded for western blot. The protein extract was later divided into two aliquots, one for IP
851 against the protein of interest (antibodies listed below) and the other for IP against IgG, and was then
852 incubated with 30 µL of Dynabeads™ Protein G (Invitrogen, #10004D) and 5 µg of antibody overnight at
853 4°C on a rotisserie tube rotator. The next day, the beads were washed four times with the same lysis
854 buffer used for IP and resuspended in 40µL of elution buffer (consisting of lysis buffer, NuPAGE
855 10X Reducing Agent [Invitrogen, #NP0009], NuPAGE LDS sample buffer at 1X final concentration

856 [Invitrogen, #NP0007]) and boiled at 95°C for 10 minutes before the samples were loaded in the
857 NuPAGE 4%–12% Bis-Tris Gels (Invitrogen, #NP0335BOX & #NP0336BOX) for further resolution and
858 western blot analysis.
859 For the IP with RNase treatment, the beads were resuspended in 400 µL of lysis buffer after the three
860 final washes and divided into two separate 1.5 ml tubes of 200 µL each. To establish the dose required to
861 remove all RNA, we tested different amounts of RNase I (Invitrogen, #EN0602) and found that 4 µL was
862 enough to render RNA undetectable both by denaturing gel and cDNA amplification. The negative
863 control was to go without RNase treatment; both were incubated at 37°C for 15 min on a rotisserie tube
864 rotator. After incubation, all the samples were washed one last time with 500 µL of lysis buffer and then
865 eluted in 20 µL of elution buffer. We used the same protocol for all the IP processed by mass
866 spectrometry.
867 The antibodies used for IP were: goat α-PUM1 (Bethyl Laboratories, #A300-201A), rabbit α-PUM2
868 (Bethyl Laboratories, #A300-202A), rabbit α-FMRP (Abcam Cambridge, #ab17722), rabbit α-AGO2
869 (Abcam Cambridge, #ab32381), rabbit α-NeuN (Thermo Fisher Scientific, #PA5-37407), rabbit α-
870 CNOT1 (Cell Signaling Technology, #44613), rabbit α-MOV10 (Bethyl Laboratories, #A301-571A),
871 rabbit α-RAPTOR (Cell Signaling Technology, #2280), rabbit α-CAD (Bethyl Laboratories, #A301-
872 374A), rabbit α-ANAPC1 (Bethyl Laboratories, #A301-653A), and rabbit α-FZR1 (Thermo Fisher
873 Scientific, #PA5-85303).
874 N.B.: The reason the inputs are separated from the IPs and then collaged is because *in vivo* we load
875 only 1% of the lysate, which we later run off the same blot of the IPs and expose the membrane to see
876 either the input (which usually appears first) or the IPs (which for some of them appear with a longer
877 exposure). This is common practice when working with *in vivo* tissues (De Maio *et al*, 2018) (Lee *et al*,
878 2008) (Rousseaux *et al*, 2018) (Di Grazia *et al*, 2021) (Jin *et al*, 2020) (Lee *et al*, 2020).
879
880 **Immunoprecipitation experiments from HEK293T and patient-derived cell lines.** HEK293T cells
881 and patient-derived fibroblasts or lymphoblastoid cells were lysed by pipetting up and down with a
882 1000µl tip in a lysis buffer consisting of 200mM $NaCl_2$, 100mM $NaPO_4$, 20mM Hepes pH 7.4, 1% Triton
883 X and complemented by 1X of Xpert Protease and 1X of Phosphatase Inhibitor Cocktail (GenDepot,
884 #P3100-100, #P3200-020). The rest of the protocol is the same as described above for mouse brain tissue,
885 except that we used 2.5 µg of primary antibody for IP.
886
887 **Co-Immunoprecipitation in-gel digestion for mass spectrometry.** Immunoprecipitated samples were
888 separated on NuPAGE 4-12% gradient SDS-PAGE (Invitrogen, #NP0335BOX & #NP0336BOX) and

889 stained with SimplyBlue (Invitrogen, #LC6060). Protein gel slices were excised and *in-gel* digestion
890 performed as previously described (Shevchenko *et al*, 2006), with minor modifications. Gel slices were
891 washed with 1:1 Acetonitrile and 100mM ammonium bicarbonate for 30 min then dehydrated with 100%
892 acetonitrile for 10 min until shrunk. The excess acetonitrile was then removed and the slices dried in a
893 speed-vacuum at room temperature for 10 minutes. Gel slices were reduced with 5 mM DTT for 30 min
894 at 56ºC in an air thermostat, cooled down to room temperature, and alkylated with 11 mM IAA for 30
895 min with no light. Gel slices were then washed with 100 mM of ammonium bicarbonate and 100%
896 acetonitrile for 10 min each. Excess acetonitrile was removed and dried in a speed-vacuum for 10 min at
897 room temperature and the gel slices were re-hydrated in a solution of 25 ng/µl trypsin in 50 mM
898 ammonium bicarbonate for 30 min on ice and digested overnight at 37 ºC in an air thermostat. Digested
899 peptides were collected and further extracted from gel slices in extraction buffer (1:2 ratio by volume of
900 5% formic acid: acetonitrile) at high speed, shaking in an air thermostat. The supernatants from both
901 extractions were combined and dried in a speed-vacuum. Peptides were dissolved in 3% acetonitrile/0.1%
902 formic acid.
903
904 **Liquid chromatography with tandem mass spectrometry (LC-MS/MS).** The Thermo Scientific
905 Orbitrap Fusion Tribrid mass spectrometer was used for peptide tandem mass spectroscopy (MS/MS).
906 Desalted peptides were injected in an EASY-Spray™ PepMap™ RSLC C18 50cm X 75cm ID column
907 (Thermo Scientific) connected to the Orbitrap Fusion™ Tribrid™. Peptide elution and separation were
908 achieved at a non-linear flow rate of 250 nl/min using a gradient of 5%-30% of buffer B (0.1% (v/v)
909 formic acid, 100% acetonitrile) for 110 minutes, maintaining the temperature of the column at 50 °C
910 during the entire experiment. Survey scans of peptide precursors are performed from 400 to 1500 *m/z* at
911 120K full width at half maximum (FWHM) resolution (at 200 *m/z*) with a 2 x 10^5 ion count target and a
912 maximum injection time of 50 ms. The instrument was set to run in top speed mode with 3-second cycles
913 for the survey and the MS/MS scans. After a survey scan, MS/MS was performed on the most abundant
914 precursors, i.e., those exhibiting a charge state from 2 to 6 of greater than 5 x 10^3 intensity, by isolating
915 them in the quadrupole at 1.6 Th. We used collision-induced dissociation (CID) with 35% collision
916 energy and detected the resulting fragments with the rapid scan rate in the ion trap. The automatic gain
917 control (AGC) target for MS/MS was set to 1 x 10^4 and the maximum injection time was limited to 35ms.
918 The dynamic exclusion was set to 45s with a 10ppm mass tolerance around the precursor and its isotopes.
919 Monoisotopic precursor selection was enabled.
920
921 **LC-MS/MS data analysis.** Raw mass spectrometric data were analyzed using the MaxQuant

922 environment v.1.6.1.0 (Cox & Mann, 2008) and Andromeda for database searches (Cox *et al*, 2011) at
923 default settings with a few modifications. The default was used for first search tolerance and main search
924 tolerance (20 ppm and 6 ppm, respectively). MaxQuant was set up to search with the reference mouse
925 proteome database downloaded from Uniprot (https://www.uniprot.org/proteomes/UP000000589).
926 MaxQuant performed the search for trypsin digestion with up to 2 missed cleavages. Peptide, site and
927 protein false discovery rates (FDR) were all set to 1% with a minimum of 1 peptide needed for
928 identification; label-free quantitation (LFQ) was performed with a minimum ratio count of 1. The
929 following modifications were used for protein quantification: oxidation of methionine (M), acetylation of
930 the protein N-terminus, and deamination for asparagine or glutamine (NQ). Results obtained from
931 MaxQuant were further analyzed using the Perseus statistical package (Tyanova *et al*, 2016) that is part of
932 the MaxQuant distribution. Protein identifications were filtered for common contaminants. Proteins were
933 considered for quantification only if they were found in at least two replicate groups. Significant
934 alterations in protein abundance were determined by ANOVA with a threshold for significance of $P <$
935 0.05 (permutation-based FDR correction). Pum1 protein interactors were later considered if they were
936 found in at least five out of six mass spec experiments for whole brain and in at least two out of three
937 experiments for each respective brain region with a fold-change of >1.5 between LFQ-PUM1-WT and
938 LFQ-IgG-WT (see **Table S1**).
939
940 **Protein-protein interaction map.** The protein-protein interaction map for the whole brain (**Figure 1A)**
941 was generated by Cytoscape (https://cytoscape.org/) (Otasek *et al*, 2019) and the interactions among the
942 Pum1 interactors were inferred from Corum (Giurgiu *et al*, 2019) and the Human Protein Atlas (Thul *et*
943 *al*, 2017) by g:GOSt which is a package of g:Profiler (https://biit.cs.ut.ee/gprofiler/gost) (Raudvere *et al.*,
944 2019). The protein-protein interaction to generate the brain region-specific map (**Figure S2B**) was
945 generated by Cytoscape.
946
947 **Protein quantification and western blot analysis.** Patient-derived lymphoblastoid, fibroblast cell lines,
948 and control cell lines were collected at 6×10^6 cell confluence and processed for protein extraction. For
949 mouse tissues, we processed either half brain (the other half was processed for RNA extraction, see
950 below) or the entire hippocampus, cortex, or cerebellum for protein extraction. Mouse tissues or cell
951 pellets were subsequently lysed with modified RIPA buffer consisting of 25 mM Tris-HCL, pH 7.6,
952 150 mM NaCl, 1.0% Tween 20, 1.0% sodium deoxycholate, 0.1% SDS, completed with 1X Xpert
953 Protease and 1X Phosphatase Inhibitor Cocktail Solutions (GenDepot, #P3100-100 & #P3200-020). Cells
954 were lysed by pipetting them up and down with a p1000 tip and then placed on ice for 20 min followed by

955 centrifugation at 14,800 rpm at 4°C for 25 minutes. Mouse brain tissues were lysed starting from a 18G 1
956 ½" (Becton Dickson, #305196) and move down to 21G 1 ½" (Becton Dickson, #305167) and finally to
957 26G 1 ½" (Becton Dickson, #305111) syringe needles by pipetting them up and down until the lysate
958 passed through the needle smoothly. Proteins were quantified by Pierce BCA Protein Assay Kit (Thermo
959 Scientific, # PI23225) and the absorbance was measured by NanoDrop OneC (Thermo Scientific).
960 Consequently, proteins were resolved by high resolution NuPAGE 4%–12% Bis-Tris Gel (Invitrogen,
961 #NP0335BOX & #NP0336BOX) according to the manufacturer's instructions. All the blots were
962 acquired on the G:BOX Chemi XX9 machine (Syngene; Frederick, MD) using GeneSys software 1.6.5.0.
963 Gel exposures were determine by the software.
964 Antibodies used for all the western blot experiments were: goat α-PUM1 [1:2500, (Bethyl
965 Laboratories, #A300-201A)], rabbit α-PUM1 [1:2000, (Abcam Cambridge, #ab92545)], rabbit α-PUM2
966 [1:2000, (Bethyl Laboratories, # A300-202A)], rabbit α-FMRP [1:1000, (Abcam Cambridge, #ab17722)],
967 rabbit α-AGO2 [1:1000, (Abcam Cambridge, #ab32381)], rabbit α-NeuN (Rbfox3) [1:1000, (Thermo
968 Scientific, #PA5-37407)], rabbit α-CNOT1 [1:1000, (Cell Signaling Technology, #44613)], rabbit α-
969 MOV10 [1:2000, (Bethyl Laboratories, #A301-571A)], and mouse α-GAPDH [1:10000, (Millipore,
970 #CB1001)].
971
972 **RNA extraction and quantitative real-time PCR (qPCR).** Human fibroblast, lymphoblastoid, and
973 respective control cell lines were harvested at 6 X 10^6 confluence prior to RNA extraction. For mouse
974 tissues, half of the whole brain (the other half was processed for protein extraction, see above) or the
975 entire hippocampus, cortex, or cerebellum were processed for RNA extraction. The RNA was collected
976 for both human cells, mouse brain and brain region tissues using the miRNeasy kit (QIAGEN, # 217004)
977 according to the manufacturer's instructions. RNA was quantified using NanoDrop OneC (Thermo Fisher
978 Scientific). cDNA was synthesized using Quantitect Reverse Transcription kit (QIAGEN, # 205313)
979 starting from 1 µg of RNA. Quantitative RT-polymerase chain reaction (qRT-PCR) experiments were
980 performed using the CFX96 Touch Real-Time PCR Detection System (Bio-Rad Laboratories, Hercules)
981 with PowerUP SYBR Green Master Mix (Applied Biosystems, #A25743). Real-time PCR runs were
982 analyzed using the comparative C_T method normalized against the housekeeping human gene *GAPDH* or
983 mouse *Gapdh*, depending on the experiment (Vandesompele *et al*, 2002).
984
985 **Protein stability assay.** HEK293T cells were seeded in 12-well plates for 24h and then transfected with
986 125 ng of either *PUM1* WT or mutant cDNA and one of the interactors using the jetPRIME Transfection
987 Reagent (Polyplus transfection, #55-132) according to the manufacturer's protocol. After 24 h cells were

988 treated with 0.1 mg/ml of cycloheximide (Fisher Scientific, #AAJ66004XF), which we considered time
989 zero. Cells were later collected after 30min, 1h, 2h, 4h and 5h of treatment and processed for protein
990 extraction and western blot analysis. Antibody: mouse α-Myc antibody [1:2000, (Cell Signaling
991 Technologies, #2276)].
992
993 **MicroRNA library construction and sequencing.** Library preparation and microRNA sequencing was
994 performed by LC Sciences according to the following criteria. Total RNA was extracted from cerebellum
995 of WT and *Pum1*$^{-/-}$ male and female at 10 weeks of age in triplicate, for a total of 12 samples using the
996 miRNeasy kit (QIAGEN, # 217004) according to the manufacturer's instructions. The total RNA quality
997 and quantity were assessed with Bioanalyzer 2100 (Agilent Technologies, Santa Clara) with RIN number
998 > 7.0. Approximately 1 µg of total RNA were used to prepare the small RNA library according to the
999 protocol of TruSeq Small RNA Sample Prep Kits (Illumina, San Diego). Then the single-end sequencing
1000 50bp was performed on an Illumina Hiseq 2500 at LC Sciences (Hangzhou, China) following the
1001 vendor's recommended protocol.
1002
1003 **MicroRNA sequencing bioinformatic analysis.** Raw reads were subjected to an in-house program,
1004 ACGT101-miR (LC Sciences, Houston) to remove adapter dimers, junk, low complexity, common RNA
1005 families (rRNA, tRNA, snRNA, snoRNA) and repeats. Subsequently, unique sequences of 18–26
1006 nucleotides in length were mapped to specific species precursors in miRBase 22.0
1007 (http://www.mirbase.org/) by BLAST search to identify known miRNAs and novel 3p- and 5p-derived
1008 miRNAs. Length variation at both 3' and 5' ends and one mismatch inside of the sequence were allowed
1009 in the alignment. The unique sequences mapping to specific species of mature miRNAs in hairpin arms
1010 were identified as known miRNAs. The unique sequences mapping to the other arm of known specific
1011 species precursor hairpins opposite the annotated mature miRNA-containing arm were considered to be
1012 novel 5p- or 3p-derived miRNA candidates. The remaining sequences were mapped to other selected
1013 species precursors (with the exclusion of specific species) in miRBase 22.0 by BLAST search, and the
1014 mapped pre-miRNAs were further BLASTed against the specific species genomes to determine their
1015 genomic locations. The last two were also defined as known miRNAs. The unmapped sequences were
1016 BLASTed against the specific genomes, and the hairpin RNA structures containing sequences were
1017 predicted from the flank 80 nt sequences using RNAfold software (http://rna.tbi.univie.ac.at/cgi-
1018 bin/RNAWebSuite/RNAfold.cgi). The criteria for secondary structure prediction were: (1) number of
1019 nucleotides in one bulge in stem (≤12), (2) number of base pairs in the stem region of the predicted
1020 hairpin (≥16), (3) cutoff of free energy (kCal/mol ≤-15), (4) length of hairpin (up and down stems +

1021 terminal loop ≥50), (5) length of hairpin loop (≤20), (6) number of nucleotides in one bulge in mature
1022 region (≤8), (7) number of biased errors in one bulge in mature region (≤4), (8) number of biased bulges
1023 in mature region (≤2), (9) number of errors in mature region (≤7), (10) number of base pairs in the mature
1024 region of the predicted hairpin (≥12), (11) percent of mature region in stem (≥80).
1025
1026 **RNA sequencing.** The Genomic and RNA Profiling Core at Baylor College of Medicine first conducted
1027 Sample Quality checks using the NanoDrop spectrophotometer and Agilent Bioanalyzer 2100. We then
1028 used Illumina TruSeq Stranded Total RNA library preparation protocol (p/n 15031048, revE, document
1029 #RS-122-9007) along with ThermoFisher's ERCC RNA Spike-In Control Mixes Protocol (publication
1030 number 4455352, rev. D). Our process is as follows:
1031 *Illumina TruSeq stranded total RNA sample preparation protocol*: Total RNA samples were
1032 normalized to 250ng each, based on picogreen quantitation, and ERCC RNA Spike-In Controls (p/n
1033 4456739) were incorporated into each sample. Using the TruSeq Stranded Total RNA Library Prep Gold
1034 Kit (p/n RS-122-2301), samples then underwent ribosomal RNA reduction and subsequently fragmented
1035 and primed with random hexamers to produce first strand cDNA. During second strand cDNA synthesis,
1036 RNA templates were removed and replaced with cDNA strands containing dUTP. The ds-cDNA was then
1037 purified using Beckman Coulter AMPure XP beads (p/n A63881).
1038 *Library preparation:* Libraries were created from the cDNA by attaching an adenosine to the 3' end
1039 and ligating unique adapters to the ends (for more information on this process, see below). The ligated
1040 products underwent 15 cycles of amplification and a final bead purification. The resulting libraries were
1041 quantitated using the NanoDrop spectrophotometer and fragment size assessed using the Agilent 2100
1042 Bioanalyzer. A qPCR assay was performed on the libraries to determine the concentration of adapter
1043 ligated fragments using the Applied Biosystems ViiA 7 Quantitative PCR instrument and a KAPA
1044 Library Quant Kit (p/n KK4824). All samples were pooled equimolarly and re-quantitated by qPCR, and
1045 also re-assessed on the Bioanalyzer.
1046 *Cluster generation by bridge amplification: HiSeq 2500 HOM.* Using the concentration from the
1047 ViiA7 qPCR machine above, 26pM of equimolarly pooled library was loaded onto three lanes of a high
1048 output v4 flowcell (Illumina p/n PE-401-4001) and amplified by bridge amplification using the Illumina
1049 cBot machine (cBot protocol: PE_HiSeq_Cluster_Kit_v4_cBot_recipe_v9.0). PhiX Control v3 adapter-
1050 ligated library (Illumina p/n FC-110-3001) is spiked-in at 2% by weight to ensure balanced diversity and
1051 to monitor clustering and sequencing performance. A paired-end 100 cycle run was used to sequence the
1052 flowcell on a HiSeq 2500 Sequencing System (Illumina p/n FC-401-4003). An average of 129 million
1053 read pairs per sample was sequenced.

1054 *End repair* converts the overhangs caused by fragmentation into blunt or polished ends. The 3' to 5'
1055 exonuclease activity of the End Repair mix removes the 3' overhangs, and polymerase activity fills in the
1056 5' overhangs.
1057 *Adenylation*: a single 'A' nucleotide is added to the 3' ends of the blunt fragments.
1058 *Adapter ligation*: an adapter is ligated to the 3' end of the DNA fragment with a corresponding 'T'
1059 nucleotide.
1060 *Absolute expression*: The absolute gene expression was calculated as DESeq2-normalized counts as
1061 previously described (Love *et al.*, 2014) (**Table S7**).
1062 *Samples*: RNAseq was performed in triplicate from whole C57BL/6J mouse brains at 3 weeks of age.
1063
1064 **Gene Set Enrichment Analysis (GSEA).** GSEA was performed as previously described (Subramanian *et*
1065 *al.*, 2005). The cumulative distribution function was conducted by performing 1000 random gene-set
1066 membership assignments. A nominal p-value < 0.01 and an FDR < 0.25 were used to assess the
1067 significance of the enrichment score (ES). HITS-CLIP data were obtained from the literature and were
1068 initially acquired as follows: Pum1 and Pum2 from neonatal murine brains (Zhang *et al.*, 2017), Fmrp
1069 from cerebellum, cortex, and hippocampus together (Maurin *et al.*, 2018), Ago2 from neocortex at
1070 embryonic day 13 (Chi *et al.*, 2009), Rbfox3 from mouse brain (age not specified) (Weyn-Vanhentenryck
1071 *et al.*, 2014), Nova from mouse brain (age not specified) (Zhang *et al.*, 2010), Ptpb2 from neocortex at
1072 embryonic day 18.5 (Licatalosi *et al.*, 2012), Mbnl2 from hippocampus at 8-12 weeks of age (Charizanis
1073 *et al.*, 2012), and Apc from mouse brain at embryonic day 14 (Preitner *et al.*, 2014). For consistency all
1074 the HITS-CLIP data were ranked according to their RPKM.
1075 For the normalized RPKM-GSEA analysis we performed RNAseq experiments (as described above),
1076 in triplicate, from WT C57BL/6 mouse brain at 3 weeks of age (we chose this age to be comparable to the
1077 other HITS-CLIP datasets) to infer the basal level of gene expression by DESeq2-normalized counts (see
1078 above). We then normalized the RPKM values by the DESeq2-normalized counts and repeated the GSEA
1079 enrichment analysis.
1080
1081 **Gene ontology analyses.** All gene ontology analyses were performed with David Gene Ontology (GO)
1082 and only categories with FDR<0.05 were considered. David GO for the Pum1 interactome considered the
1083 entire interactome as background. For GSEA HITS-CLIP targets shared among Pum1, Pum2, Fmrp,
1084 Ago2, and Rbfox3, we considered the entire set of all targetomes together as background.
1085
1086 **Myc and GST cloning procedure with in vitro immunoprecipitation (IP) assays.** Human *PUM1* full-

1087 length cDNA was amplified by PCR and subcloned in a pRK5 plasmid containing the Myc tag sequence
1088 (Addgene, pRK5-Myc-Parkin #17612) at the N-terminal by using SalI (New England Biolabs, # R3138S)
1089 and NotI (New England Biolabs, #R0189S) restriction enzymes to replace *Parkin* with *PUM1*. For GST,
1090 the human full-length *PUM1* cDNA was, again, subcloned first in the pRK5 plasmid containing the GST
1091 tag sequence (Addgene, pRK5-HA GST RagC wt, #19304) at the N-terminal by using SalI and NotI
1092 restriction enzymes to replace *RagC* with *PUM1*. Human *FMRP*, *AGO2* and *CNOT1*, full-length cDNA
1093 were cloned and contain the GST tag sequence at the N-terminal as described for GST-*PUM1*.
1094 To introduce the T1035S or R1147W mutations we used the QuikChange II XL Multi Site-Directed
1095 Mutagenesis kit (Agilent Technologies, #200521). The primers for the single mutagenesis experiments
1096 were designed by QuikChange software (Stratagene, San Diego, https://www.genomics.agilent.com/
1097 primerDesignProgram.jsp).
1098 For IP, HEK293T cells were seeded in 6-well plates for 24 h and then transfected with 250 ng of
1099 either WT or mutant PUM1 plasmid with one of the interactors using the jetPRIME Transfection Reagent
1100 (Polyplus transfection, #55-132) as per the manufacturer's protocol. pRK5-Myc empty plasmid (no
1101 cDNA) was used as a negative control. After 48 h, the cells were collected and processed for
1102 immunoprecipitation. Protein lysates were incubated overnight at 4°C with mouse α-Myc antibody
1103 (1:400, [Cell Signaling Technologies, #2276]) on a rotisserie tube rotator. The next day, the beads were
1104 washed four times with an IP lysis buffer and resuspended in 40 µL elution buffer (lysis buffer, NuPAGE
1105 10X Reducing Agent [Invitrogen, #NP0009], NuPAGE LDS sample buffer 4X [Invitrogen, #NP0007])
1106 and boiled at 95°C for 10 minutes before loading the samples in NuPAGE 4%–12% Bis-Tris Gels
1107 (Invitrogen, #NP0335BOX & #NP0336BOX) for further resolution and western blot analysis. Antibodies:
1108 mouse α-Myc antibody [1:2000, (Cell Signaling Technologies, #2276)], rabbit α-GST antibody [1:1000,
1109 (Cell Signaling Technologies, #2625)], mouse α-GAPDH [1:10000, (Millipore, #CB1001)].
1110
1111 **Primers.** For the qPCR analysis to unambiguously distinguish spliced cDNA from genomic DNA
1112 contamination, specific exon primers were designed to amplify across introns of the gene tested. The
1113 primers for all genes tested were designed with Primer3 (Koressaar & Remm, 2007; Untergasser *et al*,
1114 2012). Cloning primers were manually designed to amplify the longest spliced gene isoform tested; if
1115 there was more than one isoform according to the UCSC Genome Browser (https://genome.ucsc.edu/), we
1116 chose the longest. See **Table S8** for primer sequences.
1117
1118 **Quantification and Statistical Analysis**
1119 **Experimental Design**

1120 For protein and RNA quantification from patient-derived cell lines, we used values from at least six
1121 independent experiments with three biological replicates for each experiment. At every stage of the study,
1122 the experimenter was blinded to the identity of control and patient-derived cell lines. For example, for the
1123 data regarding both human patient-derived cell lines and mice, Experimenter #1 made a list of samples
1124 and controls to be tested, and Experimenter #2 randomized this list and re-labeled the tubes; Experimenter
1125 #2 was the only person with the key to identify the samples. These samples were then distributed to
1126 Experimenter #3 to culture the cells, then to Experimenter #1 to perform western blots and qRT-PCR, and
1127 lastly Experimenters #1 and #4 analyzed the data. Only then was the key applied to identify the samples.
1128 For mouse experiments, the experimenters were randomized and blinded as described above. The number
1129 of animals used and sex, and the specific statistical tests used, are indicated for each experiment in the
1130 figure legends. Sample size was based on previous experience using the same mice (Gennarino *et al.*,
1131 2015).
1132
1133 **Software and statistical analysis.** Statistical significance was analyzed using GraphPad Prism 8
1134 (https://www.graphpad.com/ scientific-software/prism/) and Excel Software (Microsoft). All data are
1135 presented as mean ± SEM. Statistical details for each experiment can be found in the figures and the
1136 legends. The range of expression levels in qPCR was determined from at least six independent
1137 experiments with three biological replicates by calculating the standard deviation of the **Δ**Ct (Pfaffl,
1138 2001). The range of expression levels in western blots was determined from at least six independent
1139 experiments with at least six biological replicates. P values were calculated by Student's T-test or analysis
1140 of variance with Tukey's post hoc analysis. For the IP and protein quantification in patient cell lines in
1141 **Figure 7**, we had only one PADDAS patient, so the six repeated experiments were technical replicates
1142 rather than biological replicates. We therefore calculated the statistical significance based on these
1143 technical replicates in comparison to the three biological replicates (i.e., healthy controls).
1144
1145 **References**

1146 Agarwal V, Bell GW, Nam JW, Bartel DP (2015) Predicting effective microRNA target sites in mammalian
1147 mRNAs. *Elife* 4
1148
1149 Almeida A, Bolanos JP, Moreno S (2005) Cdh1/Hct1-APC is essential for the survival of postmitotic
1150 neurons. *The Journal of Neuroscience: the Official Journal of the Society for Neuroscience* 25: 8115-8121
1151
1152 Bah MG, Rodriguez D, Cazeneuve C, Mochel F, Devos D, Suppiej A, Roubertie A, Meunier I, Gitiaux C,
1153 Curie A *et al* (2020) Deciphering the natural history of SCA7 in children. *Eur J Neurol* 27: 2267-2276
1154

1155 Blackinton JG, Keene JD (2014) Post-transcriptional RNA regulons affecting cell cycle and proliferation.
1156 *Semin Cell Dev Biol* 34: 44-54
1157
1158 Blewett NH, Goldstrohm AC (2012) A eukaryotic translation initiation factor 4E-binding protein
1159 promotes mRNA decapping and is required for PUF repression. *Molecular and Cellular Biology* 32: 4181-
1160 4194
1161
1162 Bohn JA, Van Etten JL, Schagat TL, Bowman BM, McEachin RC, Freddolino PL, Goldstrohm AC (2018)
1163 Identification of diverse target RNAs that are functionally regulated by human Pumilio proteins. *Nucleic*
1164 *Acids Research* 46: 362-386
1165
1166 Bonnemason-Carrere P, Morice-Picard F, Pennamen P, Arveiler B, Fergelot P, Goizet C, Hellegouarch M,
1167 Lacombe D, Plaisant C, Raclet V *et al* (2019) PADDAS syndrome associated with hair dysplasia caused by
1168 a de novo missense variant of PUM1. *American Journal of Medical Genetics Part A* 179: 1030-1033
1169
1170 Charizanis K, Lee KY, Batra R, Goodwin M, Zhang C, Yuan Y, Shiue L, Cline M, Scotti MM, Xia G *et al*
1171 (2012) Muscleblind-like 2-mediated alternative splicing in the developing brain and dysregulation in
1172 myotonic dystrophy. *Neuron* 75: 437-450
1173
1174 Chartier-Harlin MC, Kachergus J, Roumier C, Mouroux V, Douay X, Lincoln S, Levecque C, Larvor L,
1175 Andrieux J, Hulihan M *et al* (2004) Alpha-synuclein locus duplication as a cause of familial Parkinson's
1176 disease. *Lancet* 364: 1167-1169
1177
1178 Chen D, Zheng W, Lin A, Uyhazi K, Zhao H, Lin H (2012) Pumilio 1 suppresses multiple activators of p53
1179 to safeguard spermatogenesis. *Current Biology: CB* 22: 420-425
1180
1181 Cheng S, Gallie DR (2007) eIF4G, eIFiso4G, and eIF4B bind the poly(A)-binding protein through
1182 overlapping sites within the RNA recognition motif domains. *The Journal of Biological Chemistry* 282:
1183 25247-25258

1184 Chi SW, Zang JB, Mele A, Darnell RB (2009) Argonaute HITS-CLIP decodes microRNA-mRNA interaction
1185 maps. *Nature* 460: 479-486
1186
1187 Conboy JG (2017) Developmental regulation of RNA processing by Rbfox proteins. *Wiley Interdisciplinary*
1188 *Reviews RNA* 8
1189
1190 Cox J, Mann M (2008) MaxQuant enables high peptide identification rates, individualized p.p.b.-range
1191 mass accuracies and proteome-wide protein quantification. *Nature Biotechnology* 26: 1367-1372
1192
1193 Cox J, Neuhauser N, Michalski A, Scheltema RA, Olsen JV, Mann M (2011) Andromeda: a peptide search
1194 engine integrated into the MaxQuant environment. *J Proteome Res* 10: 1794-1805
1195
1196 Darnell JC, Richter JD (2012) Cytoplasmic RNA-binding proteins and the control of complex brain
1197 function. *Cold Spring Harb Perspect Biol* 4: a012344
1198
1199 Dassi E (2017) Handshakes and fights: the regulatory interplay of RNA-binding proteins. *Front Mol Biosci*
1200 4: 67

1201
1202 De Maio A, Yalamanchili HK, Adamski CJ, Gennarino VA, Liu Z, Qin J, Jung SY, Richman R, Orr H, Zoghbi
1203 HY (2018) RBM17 interacts with U2SURP and CHERP to regulate expression and splicing of RNA-
1204 processing proteins. *Cell Reports* 25: 726-736 e727
1205
1206 Di Grazia A, Marafini I, Pedini G, Di Fusco D, Laudisi F, Dinallo V, Rosina E, Stolfi C, Franze E, Sileri P *et al*
1207 (2021) The Fragile X mental retardation protein regulates RIPK1 and colorectal cancer resistance to
1208 necroptosis. *Cell Mol Gastroenterol Hepatol* 11: 639-658
1209
1210 Dittmann K, Mayer C, Czemmel S, Huber SM, Rodemann HP (2017) New roles for nuclear EGFR in
1211 regulating the stability and translation of mRNAs associated with VEGF signaling. *PloS one* 12: e0189087
1212
1213 Edwards TA, Pyle SE, Wharton RP, Aggarwal AK (2001) Structure of Pumilio reveals similarity between
1214 RNA and peptide binding motifs. *Cell* 105: 281-289
1215
1216 Enwerem, III, Elrod ND, Chang CT, Lin A, Ji P, Bohn JA, Levdansky Y, Wagner EJ, Valkov E, Goldstrohm A
1217 (2021) Human Pumilio proteins directly bind the CCR4-NOT deadenylase complex to regulate the
1218 transcriptome. *Rna*
1219
1220 Friend K, Campbell ZT, Cooke A, Kroll-Conner P, Wickens MP, Kimble J (2012) A conserved PUF-Ago-
1221 eEF1A complex attenuates translation elongation. *Nature Structural & Molecular Biology* 19: 176-183
1222
1223 Gallie DR (1998) A tale of two termini: a functional interaction between the termini of an mRNA is a
1224 prerequisite for efficient translation initiation. *Gene* 216: 1-11

1225 Gehman LT, Meera P, Stoilov P, Shiue L, O'Brien JE, Meisler MH, Ares M, Jr., Otis TS, Black DL (2012) The
1226 splicing regulator Rbfox2 is required for both cerebellar development and mature motor function. *Genes*
1227 *& Development* 26: 445-460
1228
1229 Gennarino VA, D'Angelo G, Dharmalingam G, Fernandez S, Russolillo G, Sanges R, Mutarelli M, Belcastro
1230 V, Ballabio A, Verde P *et al* (2012) Identification of microRNA-regulated gene networks by expression
1231 analysis of target genes. *Genome Research* 22: 1163-1172
1232
1233 Gennarino VA, Palmer EE, McDonell LM, Wang L, Adamski CJ, Koire A, See L, Chen CA, Schaaf CP,
1234 Rosenfeld JA *et al* (2018) A mild PUM1 mutation is associated with adult-onset ataxia, whereas
1235 haploinsufficiency causes developmental delay and seizures. *Cell* 172: 924-936 e911
1236
1237 Gennarino VA, Singh RK, White JJ, De Maio A, Han K, Kim JY, Jafar-Nejad P, di Ronza A, Kang H, Sayegh LS
1238 *et al* (2015) Pumilio1 haploinsufficiency leads to SCA1-like neurodegeneration by increasing wild-type
1239 Ataxin1 levels. *Cell* 160: 1087-1098
1240
1241 Gieffers C, Peters BH, Kramer ER, Dotti CG, Peters JM (1999) Expression of the CDH1-associated form of
1242 the anaphase-promoting complex in postmitotic neurons. *Proceedings of the National Academy of*
1243 *Sciences of the United States of America* 96: 11317-11322
1244

1245 Giurgiu M, Reinhard J, Brauner B, Dunger-Kaltenbach I, Fobo G, Frishman G, Montrone C, Ruepp A
1246 (2019) CORUM: the comprehensive resource of mammalian protein complexes-2019. *Nucleic Acids*
1247 *Research* 47: D559-D563
1248
1249 Goldstrohm AC, Hall TMT, McKenney KM (2018) Post-transcriptional regulatory functions of mammalian
1250 pumilio proteins. *Trends in Genetics* 34: 92-990
1251
1252 Hentze MW, Castello A, Schwarzl T, Preiss T (2018) A brave new world of RNA-binding proteins. *Nature*
1253 *reviews Molecular Cell Biology* 19: 327-341
1254
1255 Humphrey J, Birsa N, Milioto C, McLaughlin M, Ule AM, Robaldo D, Eberle AB, Krauchi R, Bentham M,
1256 Brown AL *et al* (2020) FUS ALS-causative mutations impair FUS autoregulation and splicing factor
1257 networks through intron retention. *Nucleic Acids Research* 48: 6889-6905
1258
1259 Imaizumi T, Mogami Y, Okamoto N, Yamamoto-Shimojima K, Yamamoto T (2019) De novo 1p35.2
1260 microdeletion including PUM1 identified in a patient with sporadic West syndrome. *Congenit Anom*
1261 *(Kyoto)* 59: 193-194
1262
1263 Jin Z, Feng H, Liang J, Jing X, Zhao Q, Zhan L, Shen B, Cheng X, Su L, Qiu W (2020) FGFR3 big up tri, open7-
1264 9 promotes tumor progression via the phosphorylation and destabilization of ten-eleven translocation-2
1265 in human hepatocellular carcinoma. *Cell Death Dis* 11: 903
1266
1267 Kedde M, van Kouwenhove M, Zwart W, Oude Vrielink JA, Elkon R, Agami R (2010) A Pumilio-induced
1268 RNA structure switch in p27-3' UTR controls miR-221 and miR-222 accessibility. *Nature Cell Biology* 12:
1269 1014-1020
1270
1271 Keene JD (2007a) Biological clocks and the coordination theory of RNA operons and regulons. *Cold*
1272 *Spring Harb Symp Quant Biol* 72: 157-165
1273
1274 Keene JD (2007b) RNA regulons: coordination of post-transcriptional events. *Nature Reviews Genetics* 8:
1275 533-543
1276
1277 Keene JD, Lager PJ (2005) Post-transcriptional operons and regulons co-ordinating gene expression.
1278 *Chromosome Res* 13: 327-337
1279
1280 Kenny PJ, Kim M, Skariah G, Nielsen J, Lannom MC, Ceman S (2020) The FMRP-MOV10 complex: a
1281 translational regulatory switch modulated by G-Quadruplexes. *Nucleic Acids Research* 48: 862-878
1282
1283 Kenny PJ, Zhou H, Kim M, Skariah G, Khetani RS, Drnevich J, Arcila ML, Kosik KS, Ceman S (2014) MOV10
1284 and FMRP regulate AGO2 association with microRNA recognition elements. *Cell Reports* 9: 1729-1741
1285
1286 Khalil B, Morderer D, Price PL, Liu F, Rossoll W (2018) mRNP assembly, axonal transport, and local
1287 translation in neurodegenerative diseases. *Brain Res* 1693: 75-91
1288

1289 Kim K, Hessl D, Randol JL, Espinal GM, Schneider A, Protic D, Aydin EY, Hagerman RJ, Hagerman PJ (2019)
1290 Association between IQ and FMR1 protein (FMRP) across the spectrum of CGG repeat expansions. *PloS*
1291 *One* 14: e0226811
1292
1293 Koressaar T, Remm M (2007) Enhancements and modifications of primer design program Primer3.
1294 *Bioinformatics* 23: 1289-1291
1295
1296 Lai KL, Liao YC, Tsai PC, Hsiao CT, Soong BW, Lee YC (2019) Investigating PUM1 mutations in a Taiwanese
1297 cohort with cerebellar ataxia. *Parkinsonism Relat Disord* 66: 220-223
1298
1299 Le H, Tanguay RL, Balasta ML, Wei CC, Browning KS, Metz AM, Goss DJ, Gallie DR (1997) Translation
1300 initiation factors eIF-iso4G and eIF-4B interact with the poly(A)-binding protein and increase its RNA
1301 binding activity. *The Journal of Biological Chemistry* 272: 16247-16255

1302 Lee EJ, Seo E, Kim JW, Nam SA, Lee JY, Jun J, Oh S, Park M, Jho EH, Yoo KH *et al* (2020) TAZ/Wnt-beta-
1303 catenin/c-MYC axis regulates cystogenesis in polycystic kidney disease. *Proceedings of the National*
1304 *Academy of Sciences of the United States of America* 117: 29001-29012
1305
1306 Lee JT, Wheeler TC, Li L, Chin LS (2008) Ubiquitination of alpha-synuclein by Siah-1 promotes alpha-
1307 synuclein aggregation and apoptotic cell death. *Human Molecular Genetics* 17: 906-917
1308
1309 Leeb M, Dietmann S, Paramor M, Niwa H, Smith A (2014) Genetic exploration of the exit from self-
1310 renewal using haploid embryonic stem cells. *Cell Stem Cell* 14: 385-393
1311
1312 Licatalosi DD, Yano M, Fak JJ, Mele A, Grabinski SE, Zhang C, Darnell RB (2012) Ptbp2 represses adult-
1313 specific splicing to regulate the generation of neuronal precursors in the embryonic brain. *Genes &*
1314 *Development* 26: 1626-1642
1315
1316 Lin H, Spradling AC (1997) A novel group of pumilio mutations affects the asymmetric division of
1317 germline stem cells in the Drosophila ovary. *Development* 124: 2463-2476
1318
1319 Liu GY, Sabatini DM (2020) mTOR at the nexus of nutrition, growth, ageing and disease. *Nature Reviews*
1320 *Molecular Cell Biology* 21: 183-203
1321
1322 Love MI, Huber W, Anders S (2014) Moderated estimation of fold change and dispersion for RNA-seq
1323 data with DESeq2. *Genome Biology* 15: 550
1324
1325 Lukong KE, Chang KW, Khandjian EW, Richard S (2008) RNA-binding proteins in human genetic disease.
1326 *Trends in Genetics:* 24: 416-425
1327
1328 Mandelboum S, Manber Z, Elroy-Stein O, Elkon R (2019) Recurrent functional misinterpretation of RNA-
1329 seq data caused by sample-specific gene length bias. *PLoS Biol* 17: e3000481
1330
1331 Mauger O, Lemoine F, Scheiffele P (2016) Targeted intron retention and excision for rapid gene
1332 regulation in response to neuronal activity. *Neuron* 92: 1266-1278
1333

1334 Maurin T, Lebrigand K, Castagnola S, Paquet A, Jarjat M, Popa A, Grossi M, Rage F, Bardoni B (2018)
1335 HITS-CLIP in various brain areas reveals new targets and new modalities of RNA binding by fragile X
1336 mental retardation protein. *Nucleic Acids Research* 46: 6344-6355
1337
1338 McCabe MP, Cullen ER, Barrows CM, Shore AN, Tooke KI, Laprade KA, Stafford JM, Weston MC (2020)
1339 Genetic inactivation of mTORC1 or mTORC2 in neurons reveals distinct functions in glutamatergic
1340 synaptic transmission. *Elife* 9
1341
1342 Menon KP, Sanyal S, Habara Y, Sanchez R, Wharton RP, Ramaswami M, Zinn K (2004) The translational
1343 repressor Pumilio regulates presynaptic morphology and controls postsynaptic accumulation of
1344 translation factor eIF-4E. *Neuron* 44: 663-676

1345 Miles WO, Tschop K, Herr A, Ji JY, Dyson NJ (2012) Pumilio facilitates miRNA regulation of the E2F3
1346 oncogene. *Genes & Development* 26: 356-368
1347
1348 Miller MA, Olivas WM (2011) Roles of Puf proteins in mRNA degradation and translation. *Wiley*
1349 *Interdisciplinary Reviews RNA* 2: 471-492
1350
1351 Muraro NI, Weston AJ, Gerber AP, Luschnig S, Moffat KG, Baines RA (2008) Pumilio binds para mRNA
1352 and requires Nanos and Brat to regulate sodium current in Drosophila motoneurons. *The Journal of*
1353 *Neuroscience: the Official Journal of the Society for Neuroscience* 28: 2099-2109
1354
1355 Orr HT, Zoghbi HY (2007) Trinucleotide repeat disorders. *Annual review of neuroscience* 30: 575-621
1356 Otasek D, Morris JH, Boucas J, Pico AR, Demchak B (2019) Cytoscape Automation: empowering
1357 workflow-based network analysis. *Genome Biology* 20: 185
1358
1359 Pfaffl MW (2001) A new mathematical model for relative quantification in real-time RT-PCR. *Nucleic*
1360 *Acids Research* 29: e45
1361
1362 Preitner N, Quan J, Nowakowski DW, Hancock ML, Shi J, Tcherkezian J, Young-Pearse TL, Flanagan JG
1363 (2014) APC is an RNA-binding protein, and its interactome provides a link to neural development and
1364 microtubule assembly. *Cell* 158: 368-382
1365
1366 Qiu C, Dutcher RC, Porter DF, Arava Y, Wickens M, Hall TMT (2019) Distinct RNA-binding modules in a
1367 single PUF protein cooperate to determine RNA specificity. *Nucleic Acids Research* 47: 8770-8784
1368
1369 Raudvere U, Kolberg L, Kuzmin I, Arak T, Adler P, Peterson H, Vilo J (2019) g:Profiler: a web server for
1370 functional enrichment analysis and conversions of gene lists (2019 update). *Nucleic Acids Research* 47:
1371 W191-W198
1372
1373 Ravanidis S, Kattan FG, Doxakis E (2018) Unraveling the pathways to neuronal homeostasis and disease:
1374 mechanistic insights into the role of RNA-binding proteins and associated factors. *Int J Mol Sci* 19
1375
1376 Rousseaux MWC, Tschumperlin T, Lu HC, Lackey EP, Bondar VV, Wan YW, Tan Q, Adamski CJ, Friedrich J,
1377 Twaroski K *et al* (2018) ATXN1-CIC Complex is the primary driver of cerebellar pathology in
1378 spinocerebellar ataxia type 1 through a gain-of-function mechanism. *Neuron* 97: 1235-1243 e1235
1379

1380 Rovelet-Lecrux A, Hannequin D, Raux G, Le Meur N, Laquerriere A, Vital A, Dumanchin C, Feuillette S,
1381 Brice A, Vercelletto M *et al* (2006) APP locus duplication causes autosomal dominant early-onset
1382 Alzheimer disease with cerebral amyloid angiopathy. *Nature Genetics* 38: 24-26
1383
1384 Salcedo-Arellano MJ, Dufour B, McLennan Y, Martinez-Cerdeno V, Hagerman R (2020) Fragile X
1385 syndrome and associated disorders: clinical aspects and pathology. *Neurobiology of Disease* 136: 104740
1386
1387 Sandweiss AJ, Brandt VL, Zoghbi HY (2020) Advances in understanding of Rett syndrome and MECP2
1388 duplication syndrome: prospects for future therapies. *Lancet Neurol* 19: 689-698
1389
1390 Shah S, Molinaro G, Liu B, Wang R, Huber KM, Ritcher JD (2020) FMRP control of ribosome translocation
1391 promotes chromatin modifications and alternative splicing of neuronal genes linked to autism. *Cell*
1392 *Reports* 30
1393
1394 Shevchenko A, Tomas H, Havlis J, Olsen JV, Mann M (2006) In-gel digestion for mass spectrometric
1395 characterization of proteins and proteomes. *Nature Protocols* 1: 2856-2860
1396
1397 Singh K, Gaur P, Prasad S (2007) Fragile x mental retardation (Fmr-1) gene expression is down regulated
1398 in brain of mice during aging. *Mol Biol Rep* 34: 173-181
1399
1400 Singh K, Prasad S (2008) Differential expression of Fmr-1 mRNA and FMRP in female mice brain during
1401 aging. *Mol Biol Rep* 35: 677-684
1402
1403 Sivakumar S, Gorbsky GJ (2015) Spatiotemporal regulation of the anaphase-promoting complex in
1404 mitosis. *Nature Reviews Molecular Cell Biology* 16: 82-94
1405
1406 Smidak R, Sialana FJ, Kristofova M, Stojanovic T, Rajcic D, Malikovic J, Feyissa DD, Korz V, Hoeger H,
1407 Wackerlig J *et al* (2017) Reduced levels of the synaptic functional regulator FMRP in dentate gyrus of the
1408 Aging Sprague-Dawley rat. *Front Aging Neurosci* 9: 384
1409
1410 Subramanian A, Tamayo P, Mootha VK, Mukherjee S, Ebert BL, Gillette MA, Paulovich A, Pomeroy SL,
1411 Golub TR, Lander ES *et al* (2005) Gene set enrichment analysis: a knowledge-based approach for
1412 interpreting genome-wide expression profiles. *Proceedings of the National Academy of Sciences of the*
1413 *United States of America* 102: 15545-15550
1414
1415 Takeguchi R, Takahashi S, Kuroda M, Tanaka R, Suzuki N, Tomonoh Y, Ihara Y, Sugiyama N, Itoh M (2020)
1416 MeCP2_e2 partially compensates for lack of MeCP2_e1: a male case of Rett syndrome. *Mol Genet*
1417 *Genomic Med* 8: e1088
1418
1419 Tan Q, Zoghbi HY (2019) Mouse models as a tool for discovering new neurological diseases. *Neurobiol*
1420 *Learn Mem* 165: 106902
1421
1422 Temme C, Simonelig M, Wahle E (2014) Deadenylation of mRNA by the CCR4-NOT complex in
1423 Drosophila: molecular and developmental aspects. *Front Genet* 5: 143
1424

1425 Tereshchenko A, Magnotta V, Epping E, Mathews K, Espe-Pfeifer P, Martin E, Dawson J, Duan W,
1426 Nopoulos P (2019) Brain structure in juvenile-onset Huntington disease. *Neurology* 92: e1939-e1947
1427
1428 Thul PJ, Akesson L, Wiking M, Mahdessian D, Geladaki A, Ait Blal H, Alm T, Asplund A, Bjork L, Breckels
1429 LM *et al* (2017) A subcellular map of the human proteome. *Science* 356
1430
1431 Tyanova S, Temu T, Sinitcyn P, Carlson A, Hein MY, Geiger T, Mann M, Cox J (2016) The Perseus
1432 computational platform for comprehensive analysis of (prote)omics data. *Nat Methods* 13: 731-740
1433
1434 Untergasser A, Cutcutache I, Koressaar T, Ye J, Faircloth BC, Remm M, Rozen SG (2012) Primer3--new
1435 capabilities and interfaces. *Nucleic Acids Research* 40: e115
1436
1437 Uyhazi KE, Yang Y, Liu N, Qi H, Huang XA, Mak W, Weatherbee SD, de Prisco N, Gennarino VA, Song X *et*
1438 *al* (2020) Pumilio proteins utilize distinct regulatory mechanisms to achieve complementary functions
1439 required for pluripotency and embryogenesis. *Proceedings of the National Academy of Sciences of the*
1440 *United States of America*
1441
1442 Van Etten J, Schagat TL, Hrit J, Weidmann CA, Brumbaugh J, Coon JJ, Goldstrohm AC (2012) Human
1443 Pumilio proteins recruit multiple deadenylases to efficiently repress messenger RNAs. *The Journal of*
1444 *Biological Chemistry* 287: 36370-36383
1445
1446 Vandesompele J, De Preter K, Pattyn F, Poppe B, Van Roy N, De Paepe A, Speleman F (2002) Accurate
1447 normalization of real-time quantitative RT-PCR data by geometric averaging of multiple internal control
1448 genes. *Genome Biology* 3: RESEARCH0034
1449
1450 Wamsley B, Jaglin XH, Favuzzi E, Quattrocolo G, Nigro MJ, Yusuf N, Khodadadi-Jamayran A, Rudy B,
1451 Fishell G (2018) Rbfox1 mediates cell-type-specific splicing in cortical interneurons. *Neuron* 100: 846-859
1452 e847
1453
1454 Wang X, Zamore PD, Hall TM (2001) Crystal structure of a Pumilio homology domain. *Molecular Cell* 7:
1455 855-865
1456
1457 Weidmann CA, Raynard NA, Blewett NH, Van Etten J, Goldstrohm AC (2014) The RNA binding domain of
1458 Pumilio antagonizes poly-adenosine binding protein and accelerates deadenylation. *Rna* 20: 1298-1319
1459
1460 Weyn-Vanhentenryck SM, Mele A, Yan Q, Sun S, Farny N, Zhang Z, Xue C, Herre M, Silver PA, Zhang MQ
1461 *et al* (2014) HITS-CLIP and integrative modeling define the Rbfox splicing-regulatory network linked to
1462 brain development and autism. *Cell Reports* 6: 1139-1152
1463
1464 Zamore PD, Bartel DP, Lehmann R, Williamson JR (1999) The PUMILIO-RNA interaction: a single RNA-
1465 binding domain monomer recognizes a bipartite target sequence. *Biochemistry* 38: 596-604
1466
1467 Zamore PD, Williamson JR, Lehmann R (1997) The Pumilio protein binds RNA through a conserved
1468 domain that defines a new class of RNA-binding proteins. *Rna* 3: 1421-1433
1469

1470 Zhang C, Frias MA, Mele A, Ruggiu M, Eom T, Marney CB, Wang H, Licatalosi DD, Fak JJ, Darnell RB
1471 (2010) Integrative modeling defines the Nova splicing-regulatory network and its combinatorial controls.
1472 *Science* 329: 439-443
1473
1474 Zhang M, Chen D, Xia J, Han W, Cui X, Neuenkirchen N, Hermes G, Sestan N, Lin H (2017) Post-
1475 transcriptional regulation of mouse neurogenesis by Pumilio proteins. *Genes & Development* 31: 1354-
1476 1369
1477
1478 Zoghbi HY, Bear MF (2012) Synaptic dysfunction in neurodevelopmental disorders associated with
1479 autism and intellectual disabilities. *Cold Spring Harb Perspect Biol* 4
1480
1481 Zylka MJ, Simon JM, Philpot BD (2015) Gene length matters in neurons. *Neuron* 86: 353-355

1482

Figure 1, Botta et al.

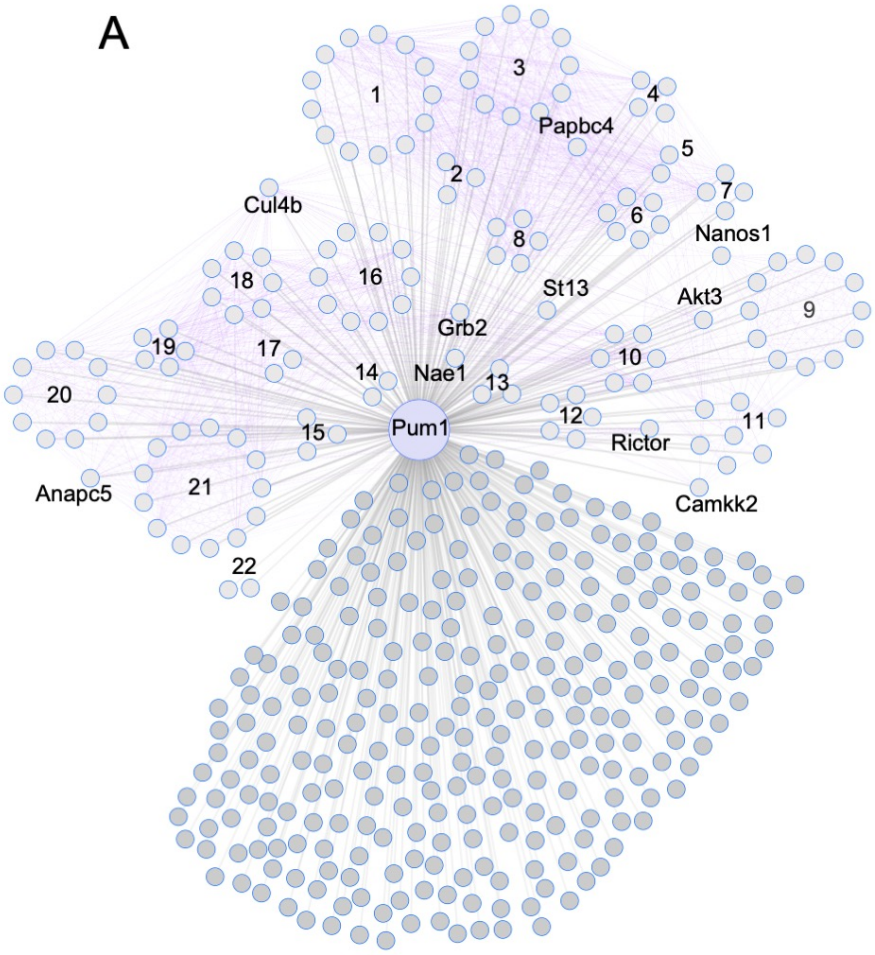

Cluster 1
Acin1
Ddx3x
Dhx15
Eftud2
Hnrnpul1
Rbm39
Sf3b3
Snrnp200
Srrt
Usp46
Wdr20
Wdr48

Cluster 2
Aff4
Mllt1
Mllt3

Cluster 3
Ctif
Eif2s1
Eif2s2
Eif2s3x
Eif2s3y
Eif3b
Eif3f
Eif3l
Eif4a3
Eif4g3
Eif5

Cluster 4
Elavl4
Etf1
Upf1
Thrap3

Cluster 5
Hnrnpa0
Hnrnpl

Cluster 6
D1Pas1
Khdrbs1
Snd1
Ssb
Ssbp2
Ssbp3

Cluster 7
Csde1
Paip1
Rae1
Rangap1

Cluster 8
Ago2
Cnot1
Fmrp
Pum2
Rbfox3

Cluster 9
Atg7
Brsk2
Fga
Fgb
Fgg
Madd
Pck2
Pex5l
Rab11fip5
Snx2
Snx4
Stxbp5l

Cluster 10
Matr3
Pfkfb2
Pfkl
Pfkm
Pfkp
Pspc1

Cluster 11
Cad
Lppr4
Lrpprc
Pten
Rptor
Tsc1
Tsc2

Cluster 12
Camk1d
Clasp1
Clip2
Rhob
Rhot1

Cluster 13
Prmt5
Rpl24
Tuba1a

Cluster 14
Kcna1
Kcna2

Cluster 15
Actbl2
Actl6b
Smarce1

Cluster 16
Cul1
Cul4a
Mycbp2
Pja1
Rlim
Rnf14
Trim32
Uba3
Uba5

Cluster 17
Pi4ka
Ttc7b

Cluster 18
Eea1
Elp3
Papss1
Pikr4
Prpsap2
Ruvbl1
Zyg11b

Cluster 19
Hdac2
Kdm1a
Ogt
Rbbp7
Zmym2

Cluster 20
Ppp1cb
Ppp1r12a
Ppp1r12b
Ppp1r12c
Ppp1r16b
Ppp1r21
Ppp2r5c
Ppp2r5d
Ppp6r1
Ppp6r2

Cluster 21
Anapc1
Anapc2
Anapc7
Anapc10
Cdc16
Cdc23
Cdc27
Cep97
Dnaja1
Fzr1
Sh3kbp1
Znf281

Cluster 22
Osbpl1
Osbpl8

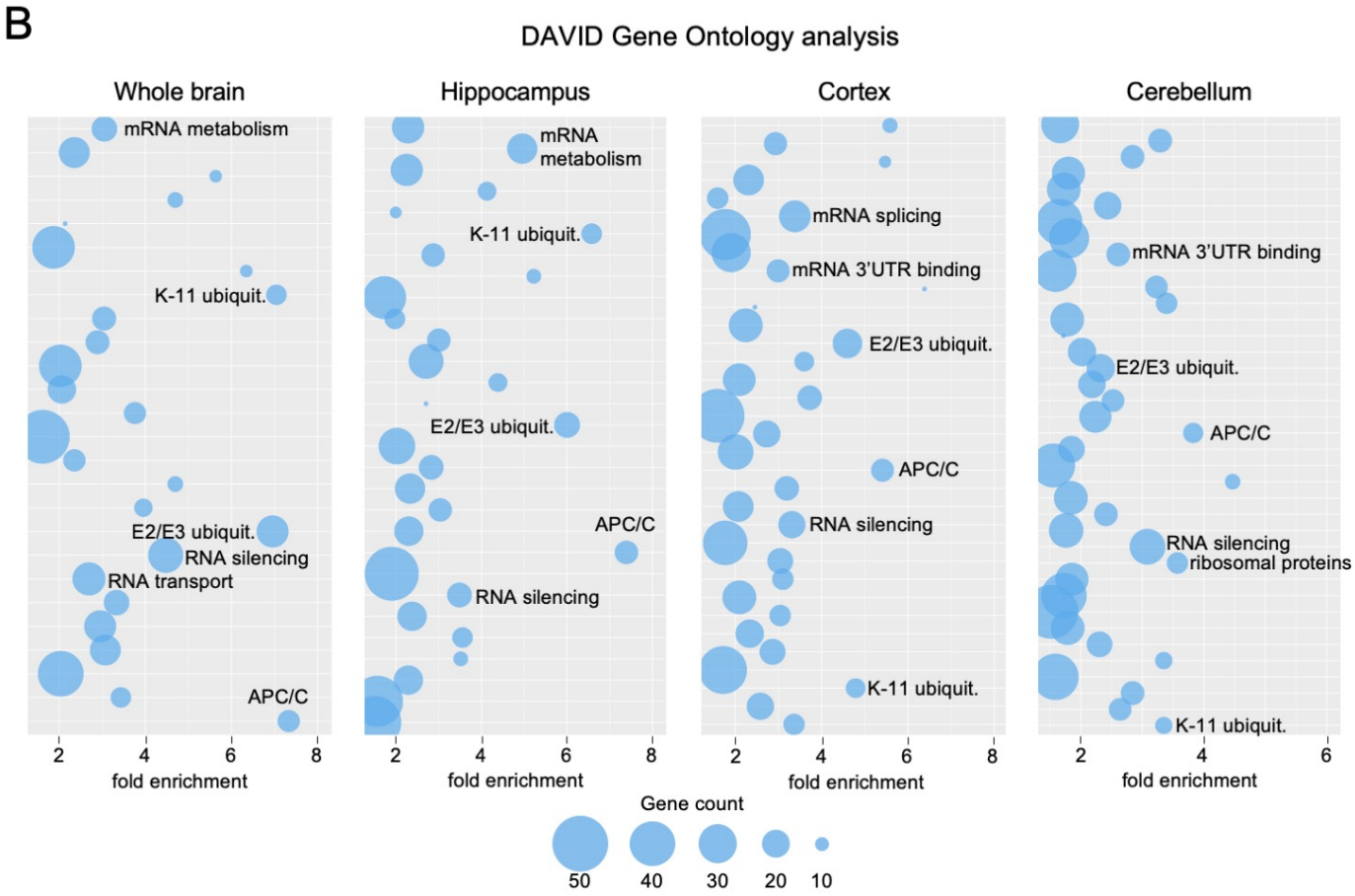

Figure 2. Botta et al.

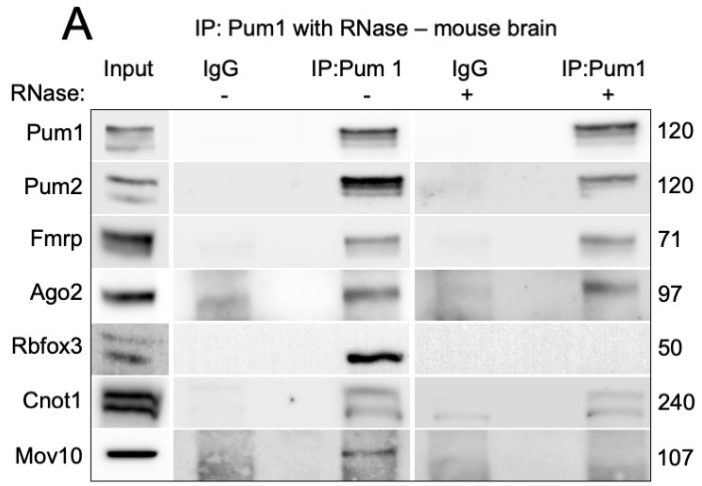

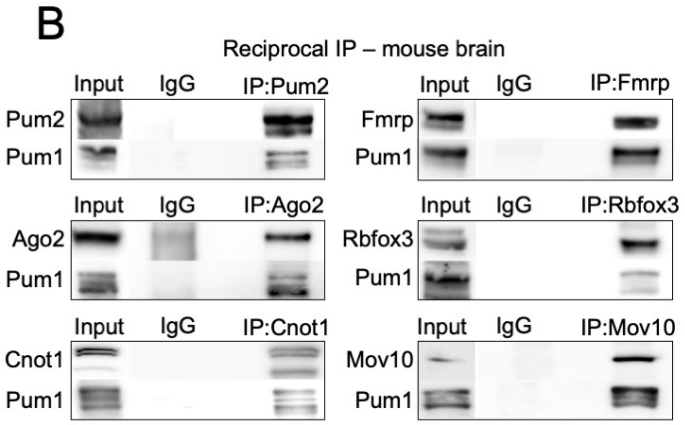

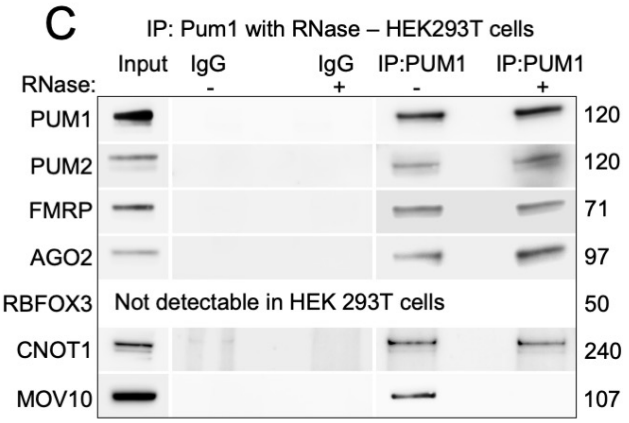

Figure 3. Botta et al.

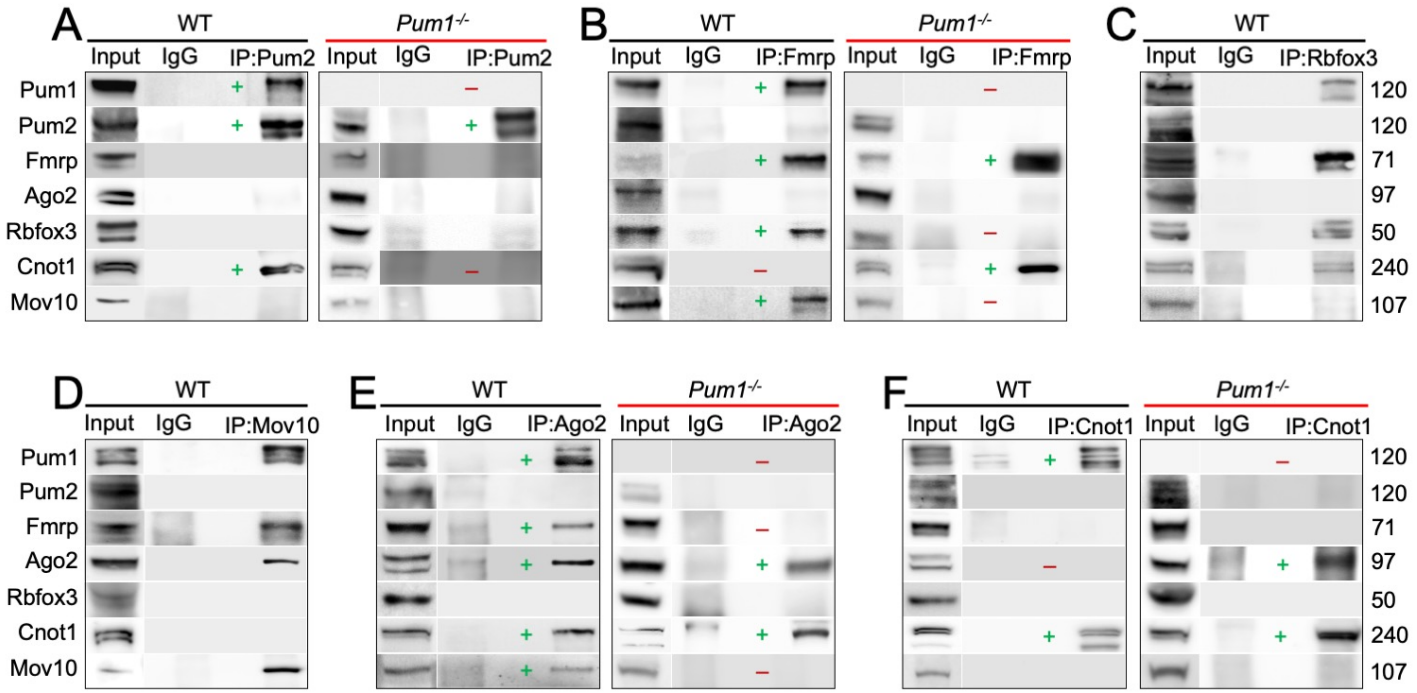

Figure 4. Botta et al.

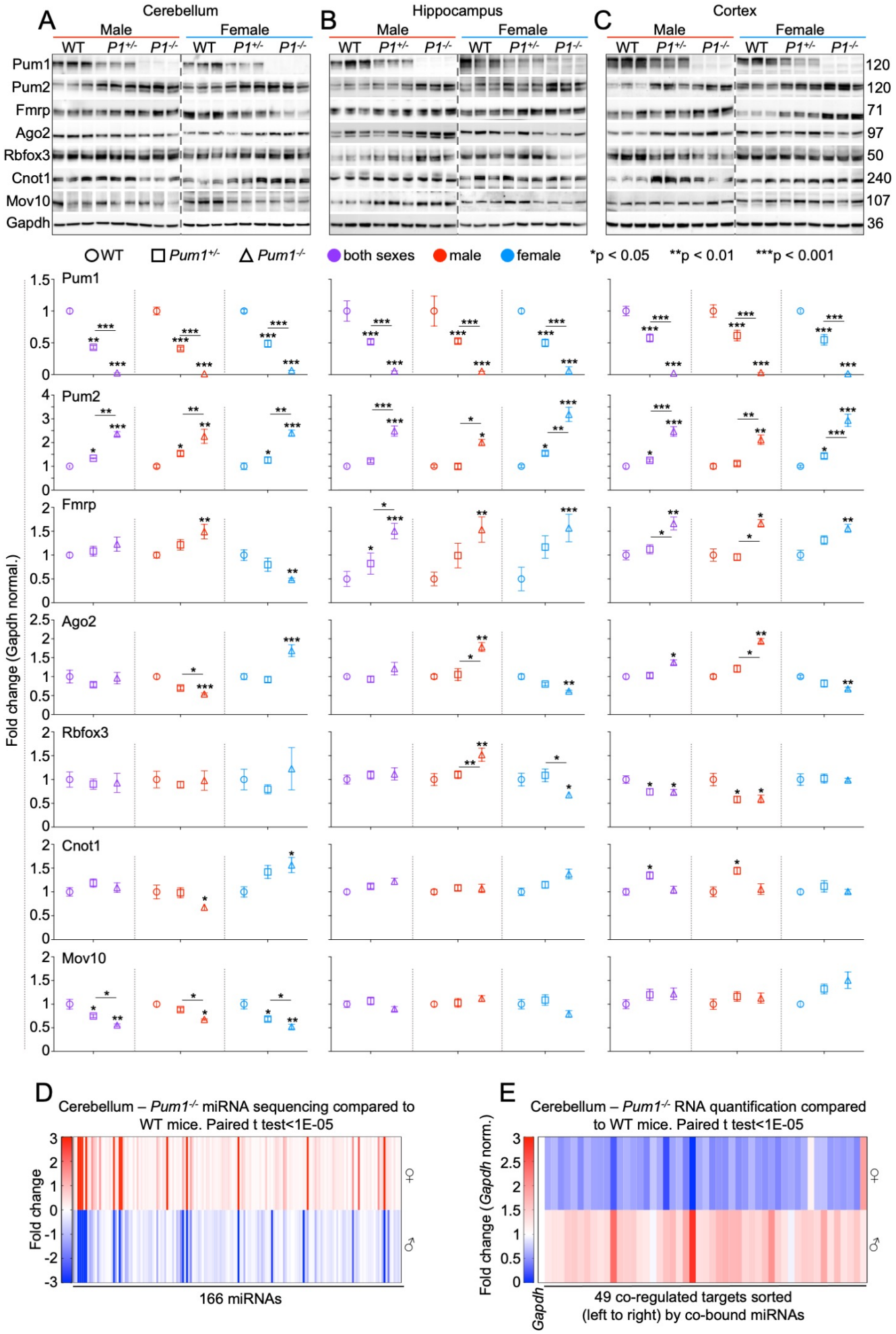

Figure 5. Botta et al.

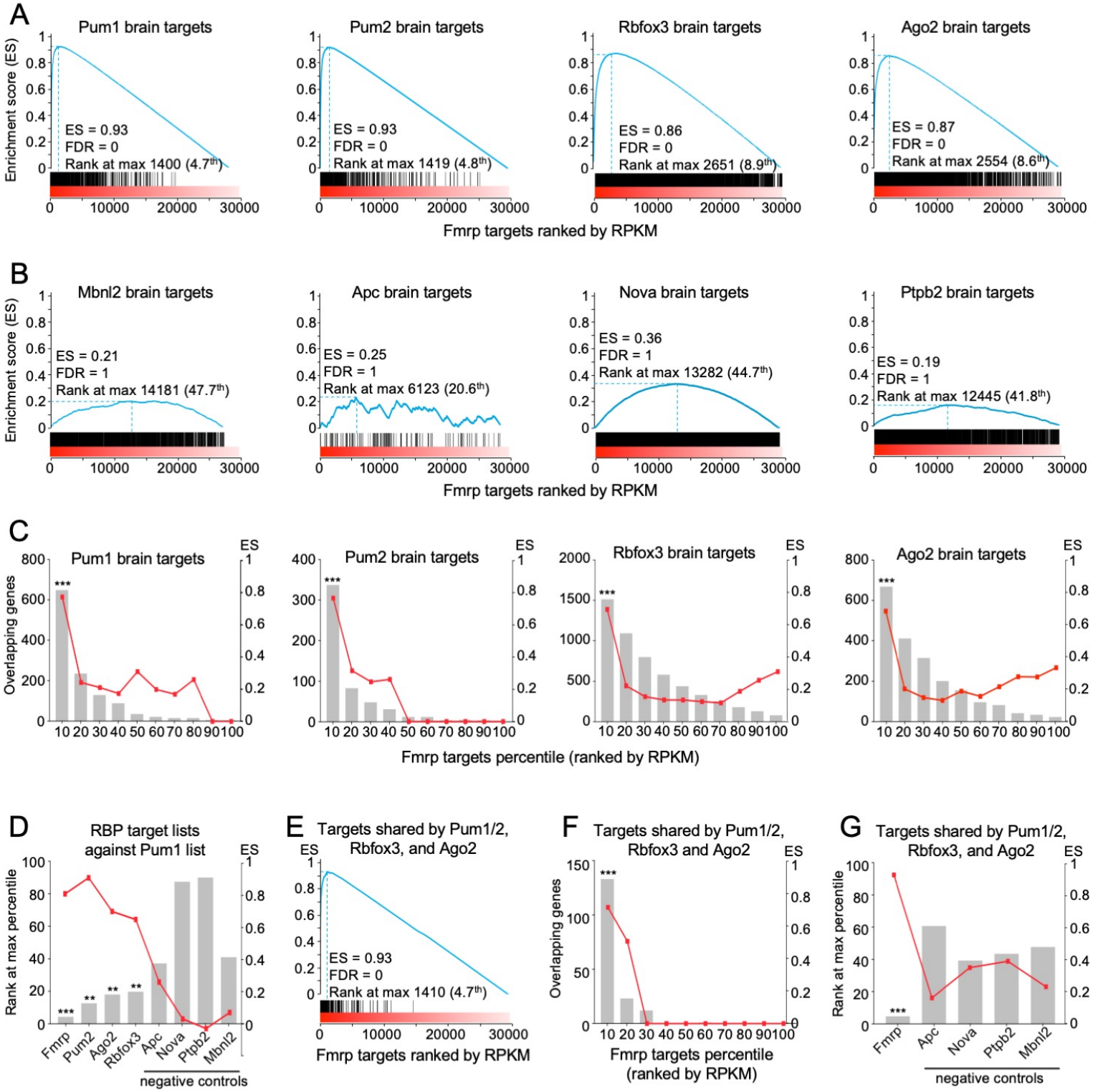

Figure 6. Botta et al.

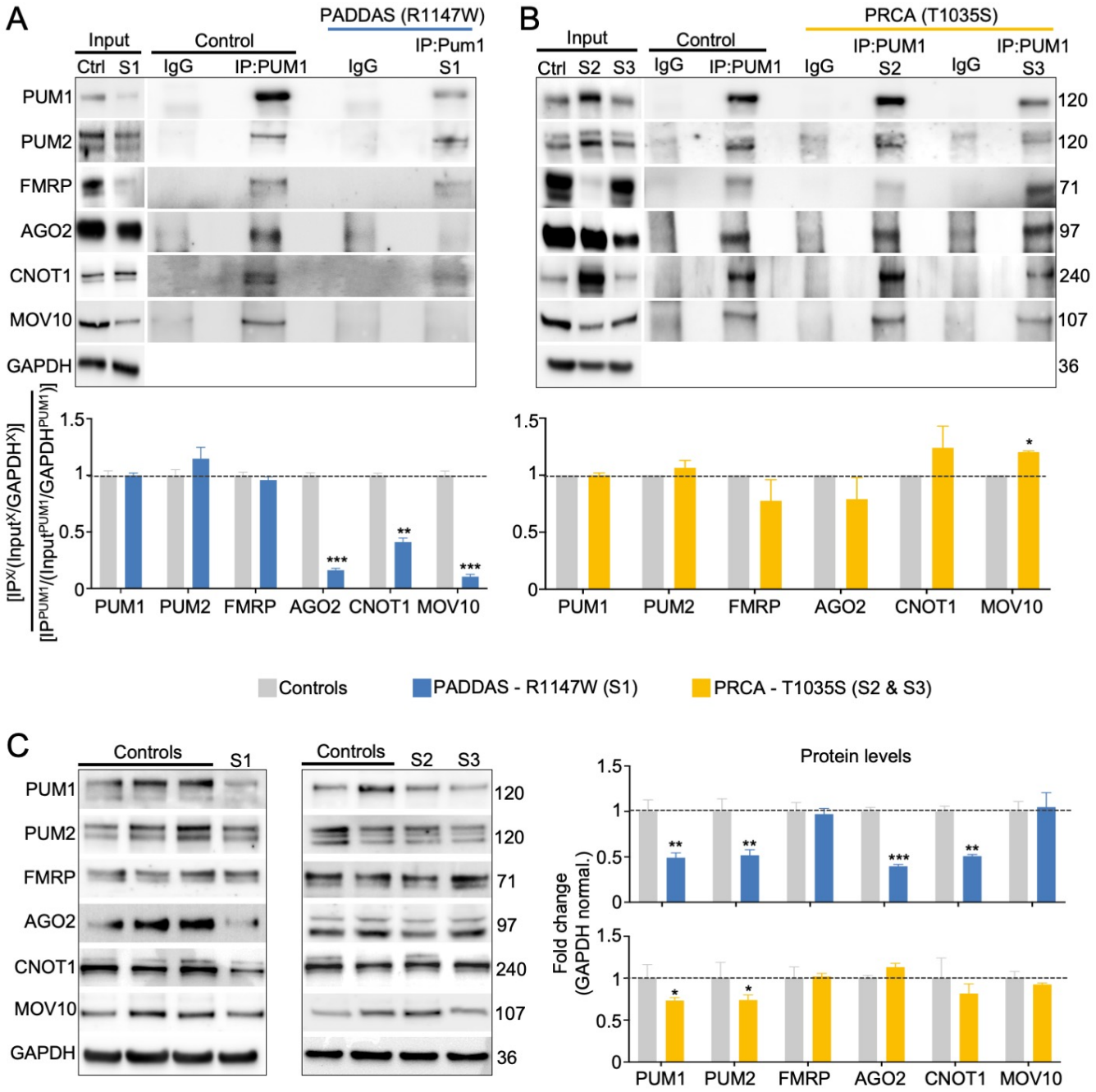

Figure 7. Botta et al.

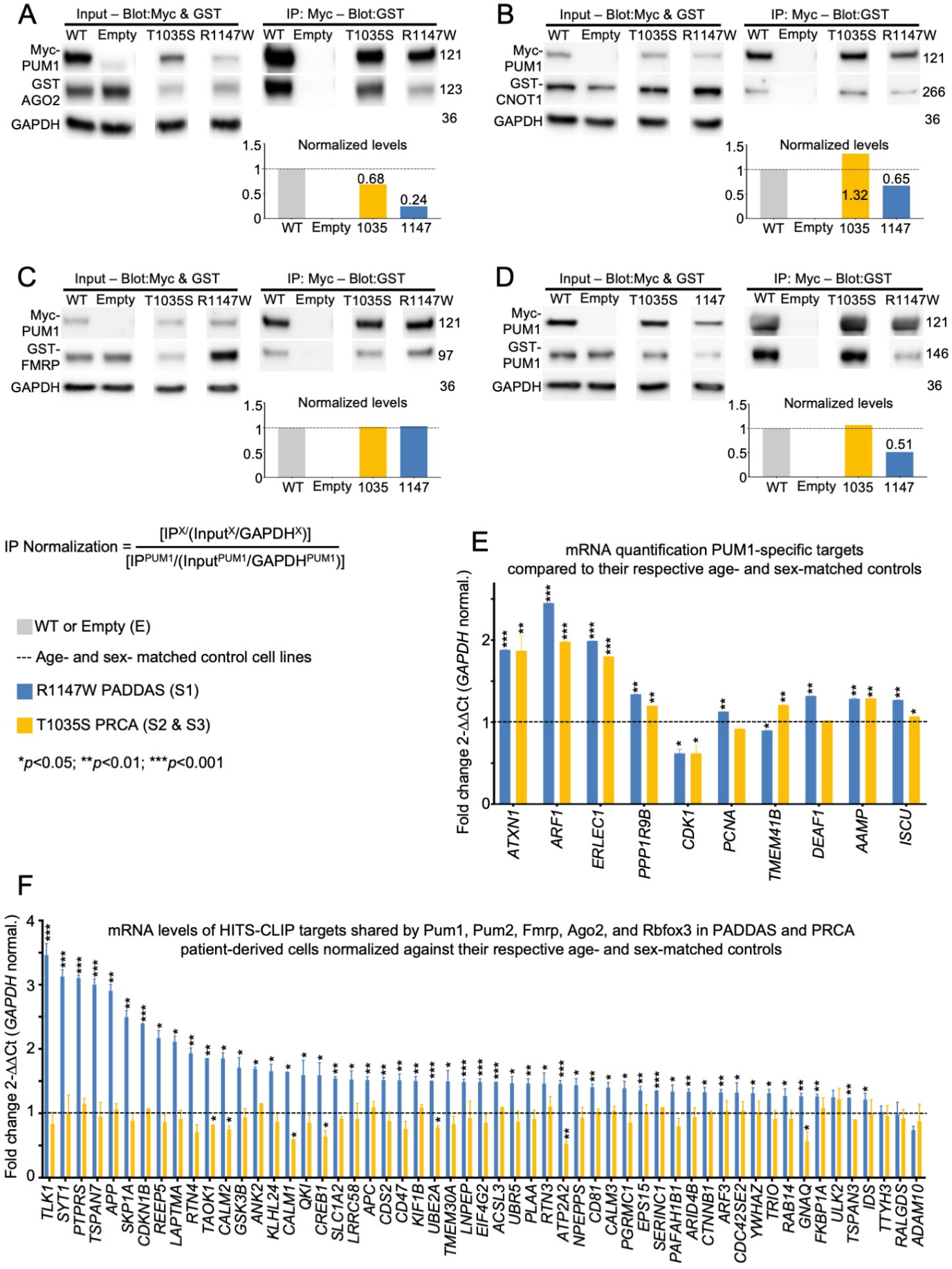

Figure S1. Botta et al.

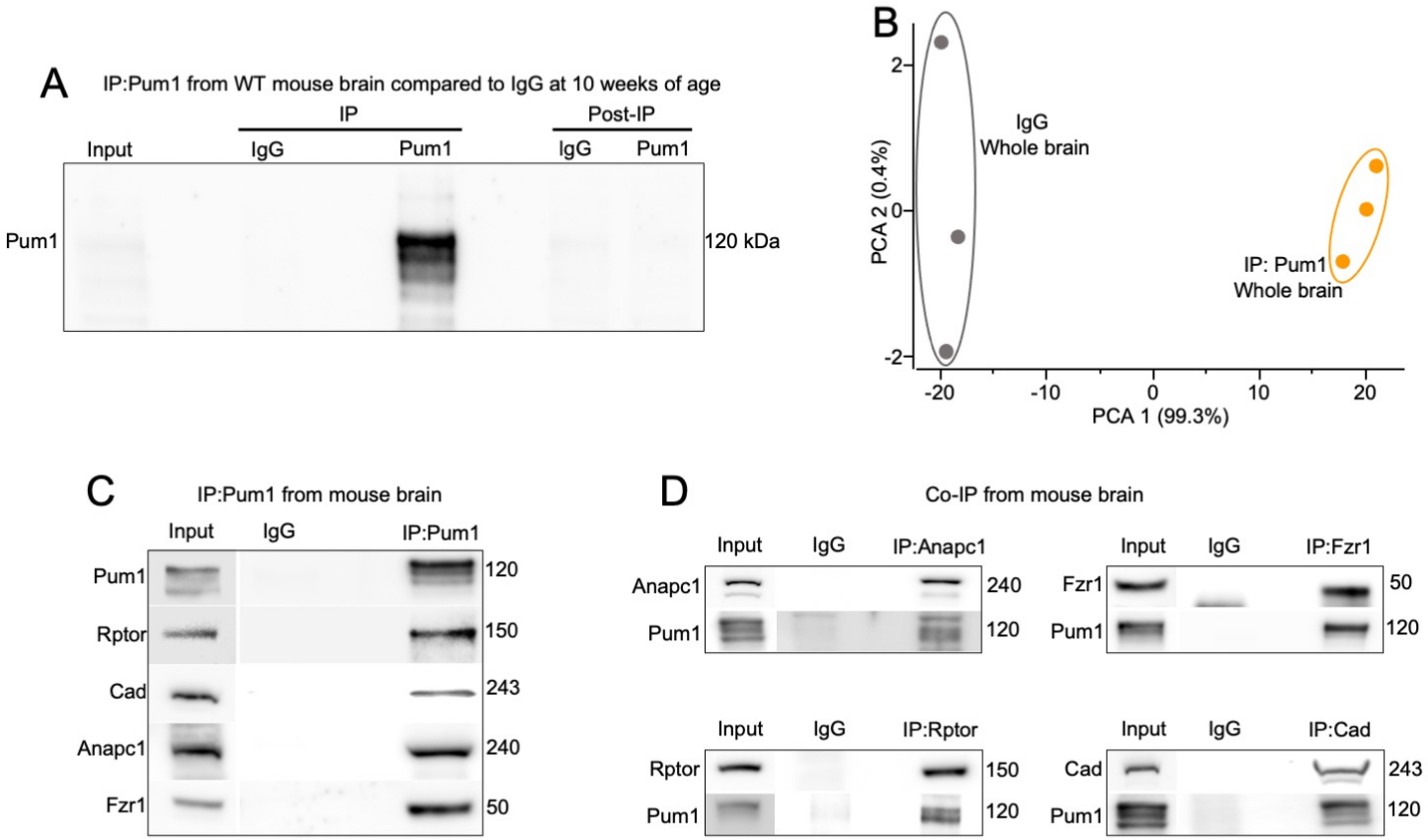

Figure S2. Botta et al.

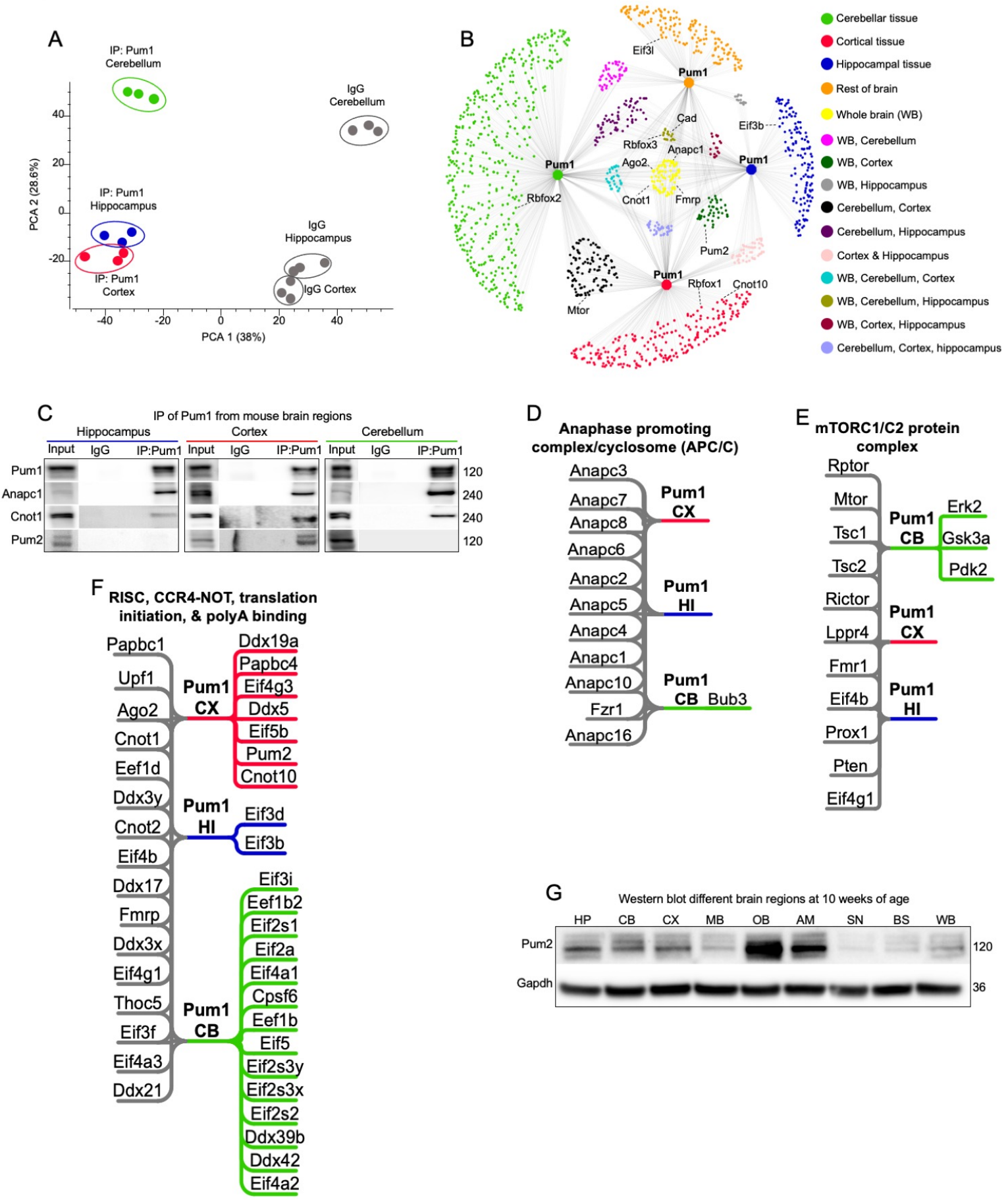

Figure S3. Botta et al.

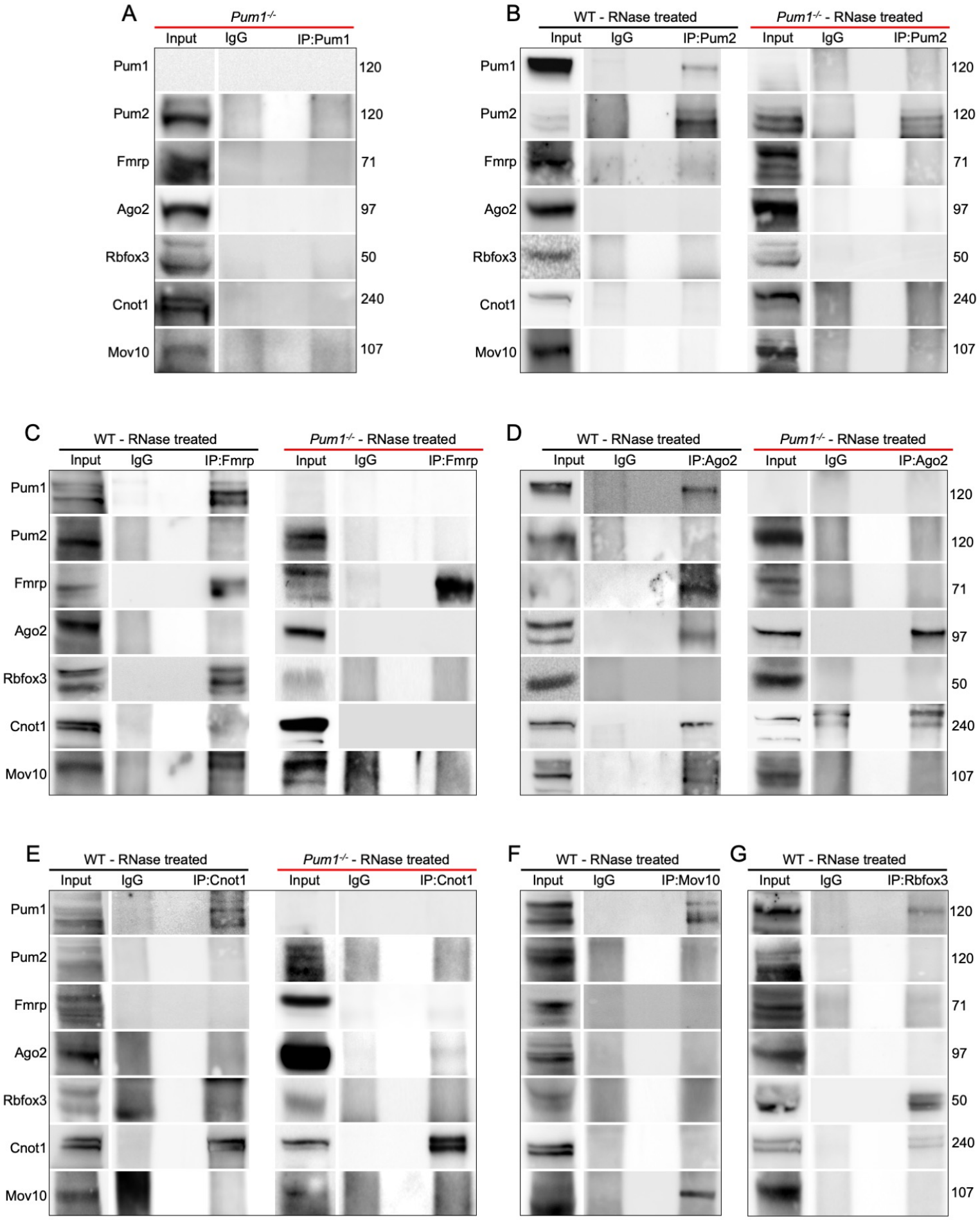

Figure S4. Botta et al.

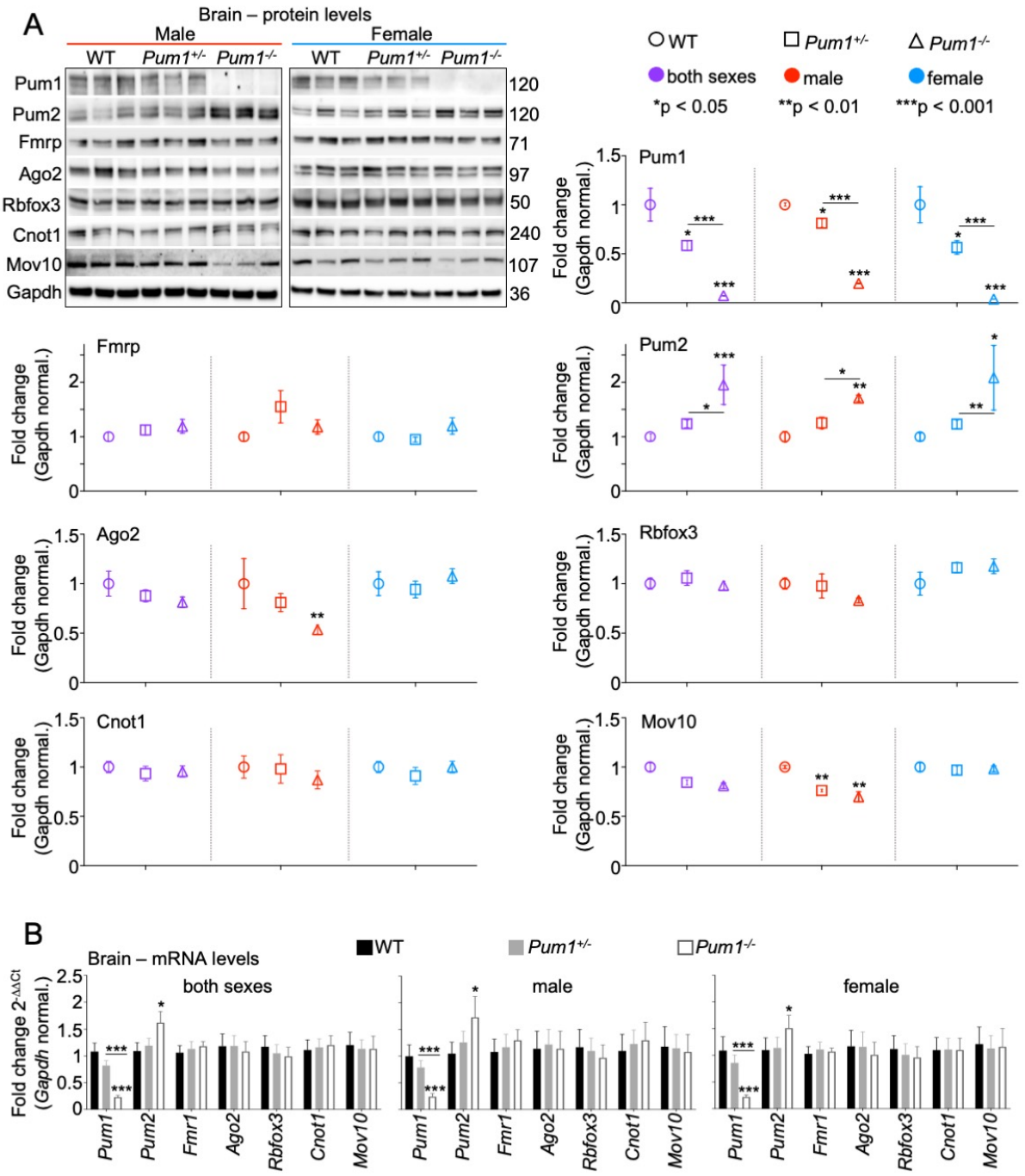

Figure S5. Botta et al.

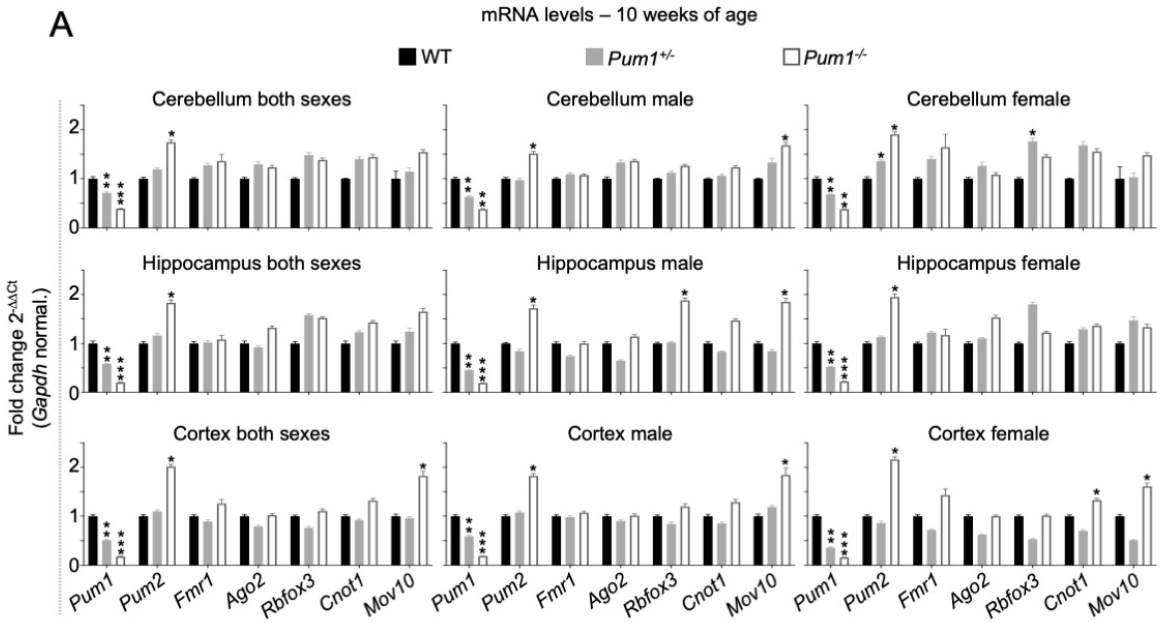

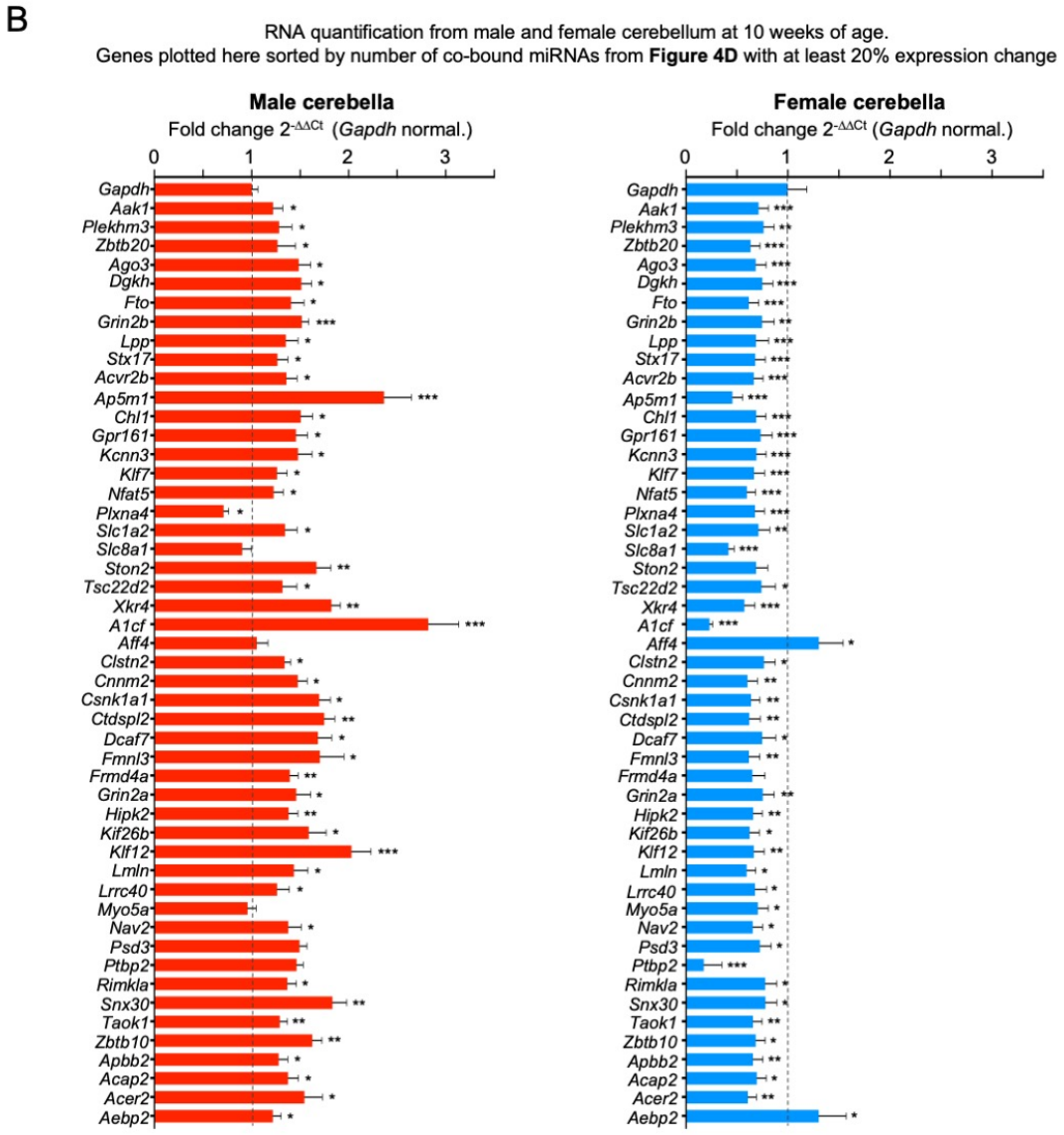

Figure S6. Botta et al.

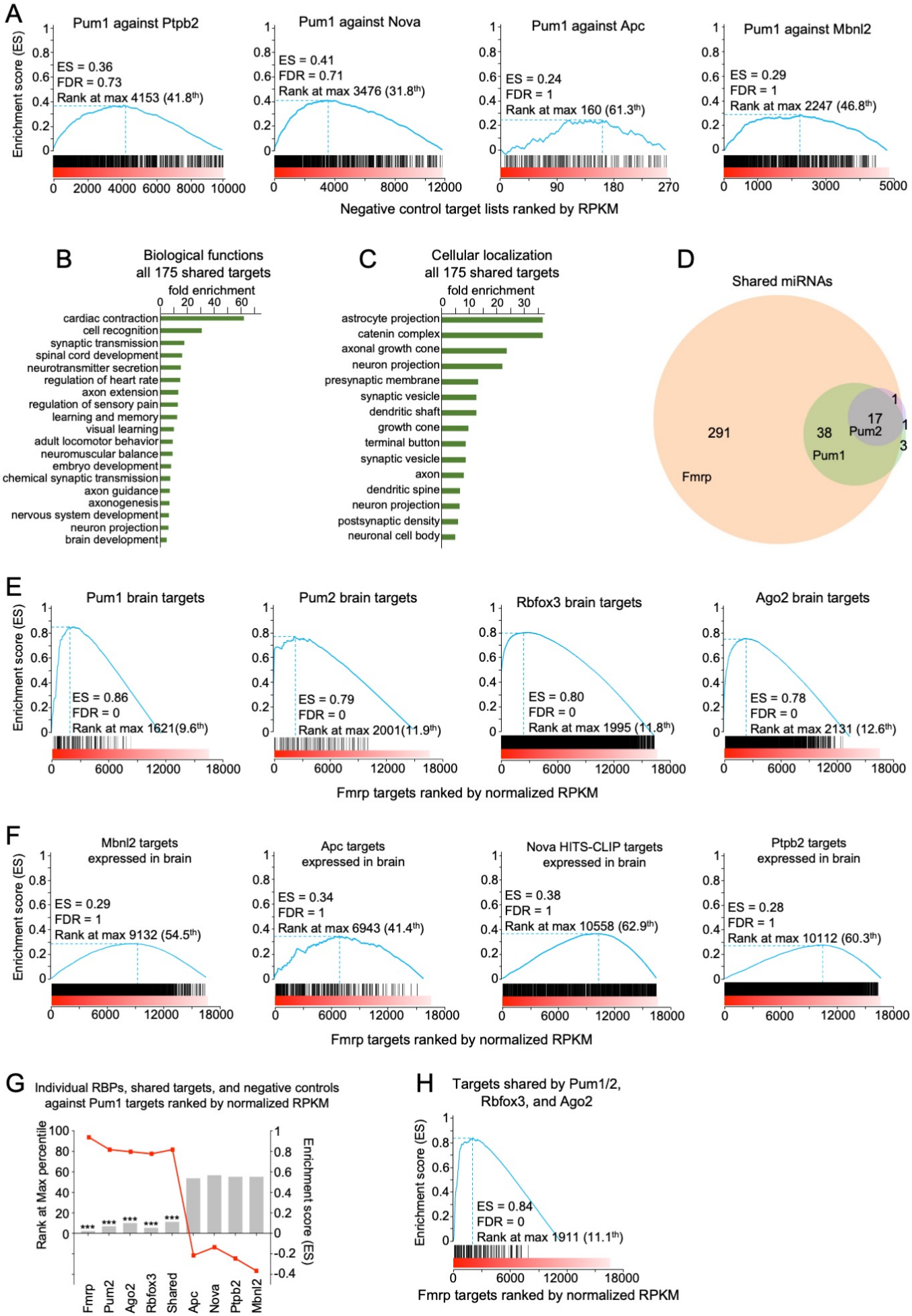
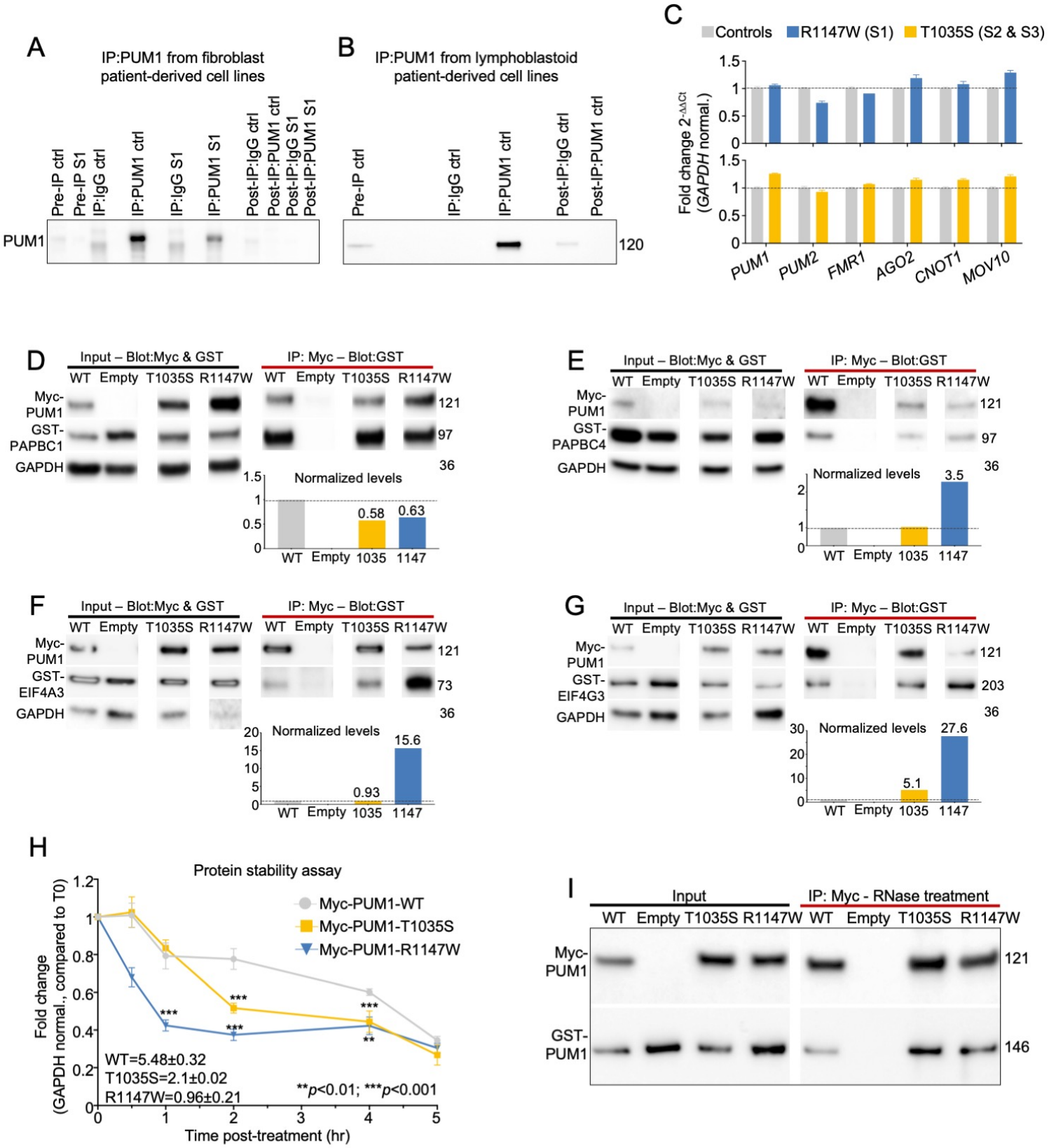
Figure S7, Botta et al.